

Semiconductor Light Source for Optical Coherence Tomography

by

Scott Elliott Webster

B.Sc.E., Queen's University, 2002

A THESIS SUBMITTED IN PARTIAL FULFILMENT OF
THE REQUIREMENTS FOR THE DEGREE OF

MASTER OF APPLIED SCIENCE

in

The Faculty of Graduate Studies

(Department of Physics and Astronomy)

We accept this thesis as conforming
to the required standard

THE UNIVERSITY OF BRITISH COLUMBIA

November 9, 2004

© Scott Elliott Webster, 2004

Abstract

Optical coherence tomography (OCT) is an emerging medical imaging technology based on the coherent interference of light. Current use of OCT in clinical settings is limited by the lack of a suitable light source. This thesis describes the design of a new type of source for OCT, based on the GaInNAs semiconductor materials system.

A semiconductor heterostructure consisting of several different quantum wells is discussed as a device for generating broadband (>100 nm) light in the near infrared (900-1500 nm). The use of temperature to control spectral shape and intensity is examined. Other aspects of device design are investigated, including models for quantum well emission and for the band gaps of dilute nitride semiconductors.

Photoluminescence measurements are presented, providing a proof of principle demonstration of the source design. Emission centred at 1225 nm with a 195 nm bandwidth is achieved. The use of temperature to control inter-well carrier transfer is demonstrated and successfully modelled. Localization effects of nitrogen cluster states are shown to be greatly reduced in quantum well structures, as compared to bulk samples.

Contents

Abstract	ii
Contents	iii
List of Tables	v
List of Figures	vi
Acknowledgements	ix
1 Introduction to Optical Coherence Tomography	1
1.1 Light Sources for OCT	3
2 Light Emission from Quantum Well Structures	5
2.1 Growth of GaAs Based Compounds by Molecular Beam Epitaxy	5
2.2 Photoluminescence	7
2.3 Nitrogen Clusters	9
2.4 The Finite Square Well	10
3 Multiple-Quantum-Well Device Design	13
3.1 Broadband Emission	13
3.2 Using Temperature to Control Emission Spectra	16

3.3	Cladding Layers	17
3.4	Stimulated Emission	22
3.5	Model for the Energy Levels in Quantum Wells	23
4	The Band Gap of Dilute Nitrides	28
4.1	Band Gap Bowing	28
4.2	GaNAs	29
4.3	GaInNAs	31
4.4	GaNAsBi	36
5	Photoluminescence Results	39
5.1	Growth Parameters	39
5.2	Description of Samples	40
5.3	Surface Oxidation	44
5.4	Experimental Procedure	48
5.5	Photoluminescence Data	50
6	Interpretation of Photoluminescence	64
6.1	Successful Broadband Emission	64
6.2	Temperature Dependence of Emission	66
6.3	Cluster State Emission	70
7	Conclusion	76
	Bibliography	78

List of Tables

5.1 Quantum well sample information.	43
--	----

List of Figures

1.1	A schematic for a typical OCT system.	2
1.2	An OCT image of the eye.	3
2.1	The finite square well potential.	11
3.1	The sum of five hyperbolic secant functions combined to produced one broadband spectrum.	15
3.2	A schematic of a double quantum well structure with GaNAs cladding layers.	19
3.3	A band diagram for a quantum well with GaNAs cladding. . .	20
3.4	Wavefunctions and ground state energy levels for the depicted well configurations with and without GaNAs cladding layers. .	21
3.5	Calculated emission spectra for various levels of gain.	24
3.6	The dependence of FWHM on gain.	25
3.7	Results of the finite square well calculations for four $\text{Ga}_{1-y}\text{In}_y\text{As}$ quantum wells.	27
4.1	Band gap map for various semiconductor alloys.	29
4.2	N K-edge absorption and emission spectra for a $\text{GaN}_{0.02}\text{As}_{0.98}$ sample.	31

4.3	Band gap dependence on nitrogen concentration, showing the agreement between photoluminescence data from our samples, published optical data by Tisch, and the LCAO model.	32
4.4	Band gap map for strained $\text{Ga}_{1-y}\text{In}_y\text{N}_x\text{As}_{1-x}$ on GaAs substrates calculated from equation 4.2 with $A = -0.47 \pm 0.10 \text{ eV}^{-1}$	35
4.5	Band gap map for strained $\text{GaN}_x\text{As}_{1-x-y}\text{Bi}_y$ on GaAs substrates using equation 4.2 with $A = 0.7 \pm 0.7 \text{ eV}^{-1}$	37
5.1	Effect of oxidation on PL intensity for samples with and without AlGaAs cladding layers.	45
5.2	PL spectra for a GaInAs quantum well sample with no cladding (1168) for different oxidation times.	47
5.3	Photoluminescence measurement setup.	48
5.4	Throughput measurements for the photoluminescence setup.	51
5.5	Photoluminescence spectra from a single GaInAs quantum well (1168) at a variety of temperatures.	53
5.6	Pulsed photoluminescence spectra from sample 1168.	54
5.7	PL spectra from a single GaInNAs quantum well (1183).	55
5.8	Pulsed PL spectra from sample 1183.	56
5.9	PL spectra from sample 1183 on an energy scale.	57
5.10	Temperature dependent PL from sample 1438, with two GaInNAs quantum wells.	58
5.11	Temperature dependent PL from sample 1437, with two GaInNAs quantum wells and one GaInAs well.	59
5.12	Temperature dependent PL from sample 1483, with two unclad GaInNAs quantum wells.	60

5.13	Temperature dependent PL from sample 1484, with two GaIn- NAs quantum wells and GaNAs cladding layers.	61
5.14	Temperature dependent PL from sample 1487, with three GaIn- NAs quantum wells.	62
5.15	Temperature dependent PL from sample 1488, with three GaIn- NAs quantum wells.	63
6.1	Photoluminescence spectra from samples 1183, 1484 and 1487; single, double and triple quantum wells, respectively.	65
6.2	Peak emission intensity relative to room temperature intensity for various samples.	67
6.3	PL from double quantum well sample 1483.	68
6.4	Ratio of low energy to high energy emission from the two quan- tum wells in sample 1438.	71
6.5	PL spectra from samples 1483 and 1484.	74

Acknowledgements

I would like to thank all the members of the MBE lab at UBC for their help and good company during my M.Sc. work. Special thanks go to Erin Young for answering numerous materials and MBE related questions, Eric Nodwell for endless aid with the computer system, Dan Beaton for many helpful discussions, and Anders Ballestad for sharing his office and “irks” with me.

Many thanks go my supervisor, Tom Tiedje, for his constant help and for providing great insight into innumerable problems. It was also handy that he managed to return from all of his crazy adventures.

Thanks to NSERC for financial support, and to David Jones for agreeing to be my second reader on short notice. Thanks to my parents for continuing to call and wish me well, even though I didn’t do such a good job of returning those calls. Thanks to Iva and Jeff for feeding me so many times, with extra thanks to Jeff for helping me break my car.

Most of all, I’d like to thank Anne. Without her support I would never have gotten this done.

Chapter 1

Introduction to Optical Coherence Tomography

Optical coherence tomography (OCT) is a medical imaging technique that uses light to look beneath the surface of the skin, into the eye, or to image other tissues. It is a candidate for future “optical biopsies” that could reduce the need for invasive surgeries for cancer diagnosis[1]. OCT is a tomographic technique that produces a three-dimensional image by analyzing the changes in waves passing through a medium (human tissue in this case). This is similar to ultrasound imaging, but with light instead of sound. The OCT system uses a Michelson interferometer to produce coherent interference between a reference beam and light reflected from the sample. Figure 1.1 shows a schematic of a typical OCT setup.

The penetration depth of light in tissue is usually limited to only a few millimeters by scattering and absorption, but this drawback is balanced by the high resolution achieved by OCT, which is usually about 1-15 μm [2]. This is at least an order of magnitude better than ultrasound, magnetic resonance, or x-ray computed tomography imaging.

High depth resolution is achieved with a low coherence light source because constructive interference will occur with the reference beam only when

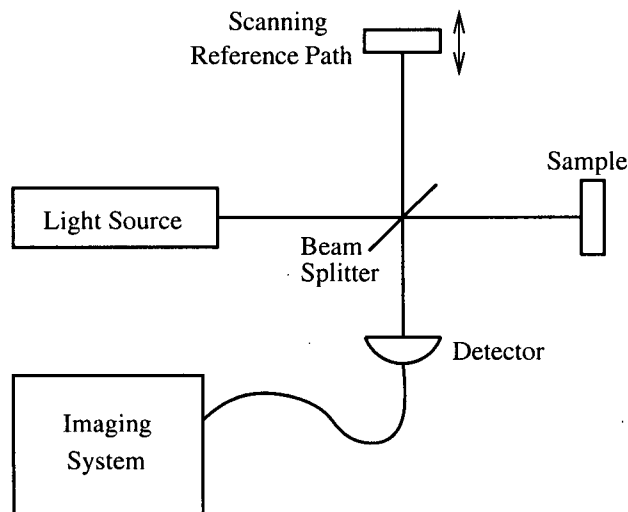


Figure 1.1: A schematic for a typical OCT system.

the path lengths are the same to within the coherence length[3]. An axial (depth) scan can be performed by changing the length of the reference beam path. Transverse scanning in the other two dimensions is accomplished by moving the light source macroscopically.

OCT is appropriate when excisional biopsies are impractical or hazardous and can lower the chance of sampling errors by allowing quick scans over larger areas[2]. OCT can be performed through an endoscope inside the body, allowing true *in situ* measurements, and does not require direct contact, nor any special transducing medium. Figure 1.2 shows a sample OCT image.

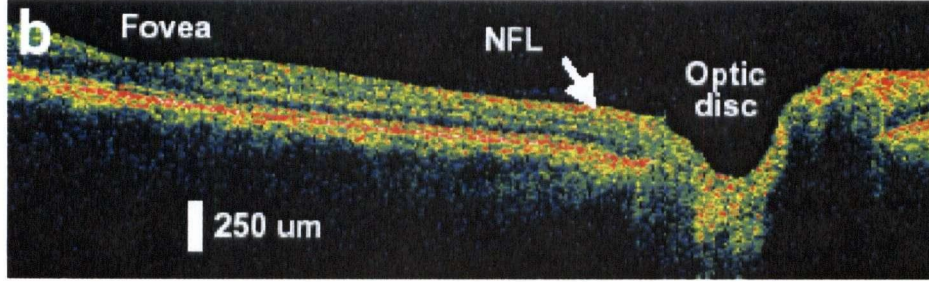


Figure 1.2: An OCT image of the eye[2].

1.1 Light Sources for OCT

The current performance of OCT systems is limited by the availability of suitable light sources. The coherence length of the source light is inversely proportional to the bandwidth of the spectrum, according to the relation

$$l_c = \frac{c}{\Delta\nu} \approx \frac{\lambda^2}{\Delta\lambda}, \quad (1.1)$$

where l_c is the coherence length, c is the speed of light, λ is the centre wavelength, and $\Delta\nu$ and $\Delta\lambda$ are the bandwidths in frequency and wavelength units, respectively[4]. Since the coherence length determines the axial resolution of the image, a broadband (low coherence length) source is necessary for optimal performance. For a Gaussian spectral distribution the resolution is[5]

$$\Delta L = \frac{2\ln 2}{\pi} \left(\frac{\lambda^2}{\Delta\lambda} \right), \quad (1.2)$$

Because penetration into tissues is limited by absorption and scattering from water and blood, a source of suitable wavelength is necessary. There are absorption minima for commonly imaged tissues in the near-infrared and scattering decreases nearly monotonically with increasing wavelength. This

leads to optimal penetration depths with sources near 1.3 or 1.65 μm [5]. The ability to use sources with varying wavelengths is also desirable because different tissues have different absorption spectra.

Other requirements are high power, which helps to achieve faster imaging (live subjects are constantly in motion) and smooth spectra, which reduce imaging artifacts in the output. Source stability, portability, and ease of use are also important design parameters.

Superluminescent diodes are often used in OCT systems. These devices typically have centre wavelengths from 850-1500 nm, bandwidths of 20-40 nm and output powers of 1-20 mW[5, 6]. In practice, resolution is limited to 15 μm . Other sources include pulsed lasers (*e.g.* Ti:Al₂O₃) and rare-earth doped fibre lasers. These lasers are large, expensive to operate, and suffer from problems due to non-ideal output with sharp spikes in the emission spectra.

This work concerns the design and construction of a new light source for OCT with a suitable emission wavelength, bandwidth and output power. The source, based on semiconductor technology, is expected to meet all the requirements for OCT while being inexpensive and convenient for clinical use.

Chapter 2

Light Emission from Quantum Well Structures

This chapter deals with the choice of materials system for the OCT light source, as well as the processes involved with light generation in semiconductors. The phenomenon of nitrogen clustering and its effects on optical properties are also introduced. The finite square well problem from quantum mechanics is reviewed as it applies to the nanoscale systems proposed for the light source.

2.1 Growth of GaAs Based Compounds by Molecular Beam Epitaxy

Gallium Arsenide (GaAs) is a technologically important direct band gap III-V semiconductor widely used in optical components. GaAs based semiconductor samples for the OCT source were grown by molecular beam epitaxy (MBE). MBE is a process where thermal beams of atoms or molecules are directed at a crystalline substrate in an ultra-high vacuum chamber[7]. MBE allows precise control of growth, down to individual atomic layers. This performance is achieved through the ability to grow at rates around one μm per

hour and through the use of shutters to block or start the beam in a fraction of second.

Since MBE growth takes place at temperatures of about half the melting point of the substrate, in theory, better quality material can be achieved than in bulk crystals due to lower densities of thermodynamic defects. Low-temperature growth also allows the production of meta-stable crystals that would normally phase separate but are kinetically stable under MBE conditions. This means that large amounts of alloying elements can be added with relative ease.

Two important alloying elements for GaAs are indium and nitrogen. Both lower the band gap of the semiconductor when added to GaAs, which allows the production of customized devices. In particular, the addition of nitrogen causes an anomalously large modification of the band gap, orders of magnitude greater than the corresponding change due to indium[8]. Unfortunately nitrogen has detrimental effects on the electronic properties of the material. Alloying elements affect the lattice constant of the crystal, but In and N have opposing effects since InAs has a higher lattice constant than GaAs, whereas GaN has a lower lattice constant. With the addition of both In and N, small band gap epitaxial layers can be grown that are lattice matched to GaAs. For an overview of the electronic properties of $\text{Ga}_{1-y}\text{In}_y\text{N}_x\text{As}_{1-x}$, see Buyanova's review[9].

The use of a surfactant during growth can improve crystal quality. Surfactants lower the free energy of the surface, which can modify the growth kinetics[10]. Bismuth is an ideal surfactant for GaInNAs growth as it does not incorporate under standard growth conditions and has many beneficial

effects. Surface roughness is reduced by an order of magnitude, nitrogen incorporation is increased, and photoluminescence intensity (discussed in the following section) can more than double[11].

The optical band gap of GaInNAs can easily be adjusted to permit emission in the wavelength range relevant to OCT, namely 900-1500 nm. This overlaps with the wavelength bands of interest for telecommunications, which is another market for GaInNAs devices. In principle, GaInNAs semiconductor alloys provide an inexpensive, compact, and convenient route to an ideal OCT light source.

2.2 Photoluminescence

Luminescence is the emission of optical radiation from an atomic or molecular system in the course of a decay from an excited state to a lower energy. The initial excitation can come from a variety of external energy sources, and in the case of an optical source, the emission process is called photoluminescence (PL). Other forms of luminescence include cathodoluminescence (electron bombardment), chemiluminescence (chemical reaction), electroluminescence (electric field) and sonoluminescence (sound)[4].

For PL in semiconductors, the incoming photons excite electrons from the valence band to the conduction band, creating an electron-hole pair. There are a variety of ways for the pair to recombine, some of which are non-radiative. The efficiency of radiative recombination can vary widely with material purity and other factors. As a result of energy conservation, emitted PL photons cannot have an energy higher than the excitation photon (unless

multiple excitation photons act together). Sometimes carriers can become stuck in localized states in the band gap (called traps) for some time, delaying or quenching luminescence.

Analysis of PL gives information about the electronic structure of samples, including the optical band gap. The high energy side of the emission spectrum comes from electrons thermally excited into higher levels in the conduction band. The shape is proportional to a Boltzmann distribution (at least for relatively high temperatures $> \sim 100$ K) given by

$$f(E) = Ae^{-\frac{E}{k_b T}}, \quad (2.1)$$

where E is the photon energy and $f(E)$ is the distribution function. Emission at energies below the band gap is also possible, due to structural inhomogeneities and thermal fluctuations in the crystal lattice. The low energy emission can be modelled with an Urbach edge[12] multiplied by a Boltzmann distribution:

$$f(E) = \alpha_g e^{\frac{E-E_g}{E_0}} e^{-\frac{E-E_g}{k_b T}}, \quad (2.2)$$

where α_g is the 0 K absorption coefficient at the optical band gap energy E_g , and E_0 is the Urbach parameter. For GaAs, α_g is 8000 cm^{-1} [13] and E_0 is 7.5 meV at room temperature[12].

Electronic properties of a sample can easily be investigated by exciting the sample with a laser of suitably low wavelength and collecting the emitted light with a spectrometer.

2.3 Nitrogen Clusters

Nitrogen clustering is an important occurrence in dilute nitride semiconductors. Various arrangements of nitrogen atoms in the crystal lattice affect the electronic and optical properties of the material.

Thomas and Hopfield reported the discovery of absorption and emission lines from pairs of nitrogen atoms in GaP in 1966[14]. One spectral line was identified as arising from an exciton bound to an isolated nitrogen atom substituted for a phosphorus atom (the A line). A series of nearby lines was then identified with nitrogen pairs in different geometric configurations (called the NN lines). These nitrogen pairs are important because they could lead to bound states in the band gap of the semiconductor.

In 1990, Liu observed similar nitrogen pair complexes in GaAs by applying pressure to the crystal[15]. This allowed the band structure of GaAs to be tuned relative to the excitonic states, revealing the pair lines. Since then, more complicated groups of N atoms have been reported[16–18]. These “nitrogen cluster states” can, depending on the configuration, lead to bound states in the band gap. These states have been studied by pseudopotential calculations[19–23] as well as experiments, including growing single atomic layers of GaNAs and observing the variation of NN line intensity with layer separation[24]. Theory[25] and experiment[26] show that nitrogen tends to incorporate substitutionally on arsenic sites in the lattice, rather than interstitially.

Cross sectional scanning tunneling microscopy studies have been conducted on GaNAs grown by metal organic vapour phase epitaxy (MOVPE)[27, 28]. These experiments determined that the distribution of N atoms was

roughly statistical, with some preference for nearest-neighbour pairing. Nitrogen clustering behaviour in MBE grown material is unknown, but could be similar to that observed for MOVPE.

Some nitrogen cluster states act as radiative recombination centres in the band gap. Excitons bound to localized states are more likely to radiate because the electron and hole are closer together. Emission from lower energy cluster states leads to broadening of the PL spectrum, and can in some cases dominate emission[29]. These localized states also affect the temperature dependence of the band gap, generally reducing the blueshift (compared to GaAs) as the temperature is lowered[29–35]. Nitrogen clusters will likely play a role in the performance of an OCT source based on GaInNAs. Their tendency to broaden emission spectra may even be a useful feature.

2.4 The Finite Square Well

The use of MBE makes it possible to grow crystals with thin layers of material of a different band gap sandwiched between thicker layers of the host crystal. These regions are small enough to exhibit quantum effects. The variation of the band gap as a function of thickness is a physical embodiment of the widely studied finite square well problem from quantum mechanics[36].

The quantum mechanical finite square well problem, in one dimension, consists of an area of reduced potential, or well, surrounded by finite-sized potential barriers. Following Weisbuch and Vinter[37], the potential has the form

$$V(x) = \begin{cases} -V_0, & \text{for } -\frac{L}{2} < x < \frac{L}{2}, \\ 0, & \text{for } |x| > \frac{L}{2}, \end{cases} \quad (2.3)$$

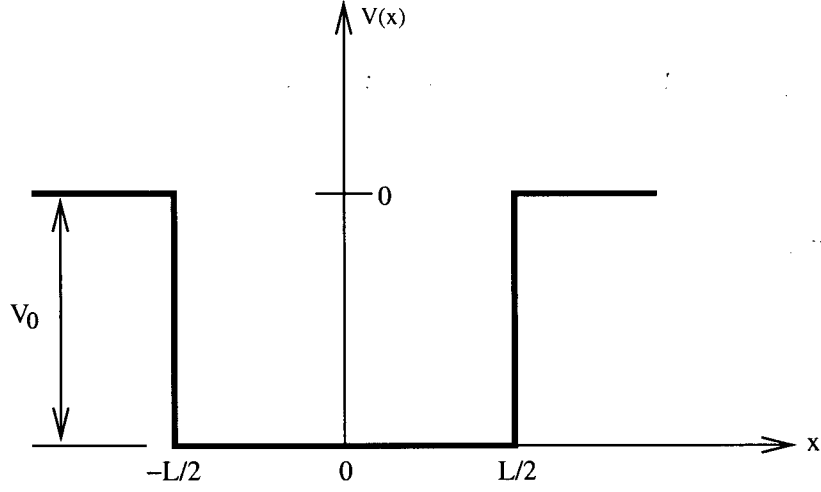


Figure 2.1: The finite square well potential.

as shown in figure 2.1.

The appropriate time-independent Schrödinger equation is

$$-\frac{\hbar^2}{2m_{b,w}^*} \frac{d^2\psi}{dx^2} + V(x) = E\psi, \quad (2.4)$$

with even solutions for this potential of

$$\psi(x) = \begin{cases} A \cos(kx), & \text{for } |x| < \frac{L}{2} \\ B e^{-\kappa(x - \frac{L}{2})}, & \text{for } x > \frac{L}{2} \\ B e^{+\kappa(x + \frac{L}{2})}, & \text{for } x < -\frac{L}{2} \end{cases} \quad (2.5)$$

that satisfy the boundary conditions where

$$\kappa \equiv \frac{\sqrt{-2m_b^* E}}{\hbar}, \quad (2.6a)$$

$$k \equiv \frac{\sqrt{2m_w^* (E + V_0)}}{\hbar}, \quad (2.6b)$$

E is the energy of the state, and $m_{b,w}^*$ are the barrier and well effective masses, respectively. There are also odd solutions, with \sin instead of \cos in equation 2.5.

Continuity conditions for the wavefunction and its derivative dictate that

$$A \cos\left(\frac{kL}{2}\right) = B \quad (2.7)$$

and

$$\left(\frac{k}{m_w^*}\right) \sin\left(\frac{kL}{2}\right) = \frac{\kappa B}{m_b^*}. \quad (2.8)$$

Dividing equations 2.7 and 2.8 gives

$$\left(\frac{k}{m_w^*}\right) \tan\left(\frac{kL}{2}\right) = \frac{\kappa}{m_b^*}. \quad (2.9)$$

This transcendental equation, and the similar one corresponding to the odd solutions, can be solved numerically. The roots are the energies of the states in the well. The solution can be compared to the energy levels of the infinite square well, where

$$E_n = \frac{\hbar^2}{2m_w^*} \left(\frac{n\pi}{L}\right)^2, \quad n = 1, 2, 3, \dots \quad (2.10)$$

To calculate the finite square well levels for a semiconductor quantum well structure, one needs to know the depth and width of the well, as well as the effective mass of the particle in question (electron or hole) in both the well material and that of the barrier. Other parameters, such as elastic constants and deformation potentials, are also required, in order to calculate the effect of strain for instance.

Chapter 3

Multiple-Quantum-Well Device Design

The OCT source design is described in this chapter. Various techniques for achieving the required spectral shape and output power are discussed along with a quantum well model for predicting emission wavelengths.

3.1 Broadband Emission

Multiple-quantum-well structures are a common configuration for light emitting devices. Typically the wells are identical and the structure is a simple alternation between two materials, such as GaAs and $\text{Al}_x\text{Ga}_{1-x}\text{As}$. The system is referred to as a superlattice if the wells are close enough together to allow tunneling, or communication, to occur between the wells[37].

When electron-hole pairs are formed in a multiple-quantum-well structure by some form of excitation, the carriers usually migrate into the wells since they have a lower band gap than the surrounding material and are therefore energetically favourable. If these carriers radiatively recombine, the energy of the emitted photons is determined by the characteristics of the quantum wells. If all the wells are the same, then the emission spectrum is generally

a relatively sharp line at a specific wavelength. If some of the wells were modified, causing a change in the confinement energy of the electrons or holes, then one could expect the emission spectrum to correspond to a combination of different emission lines.

The semiconductor OCT source design consists of a series of different quantum wells, all emitting at nearby wavelengths, arranged in such a way so as to produce a smooth, broadband spectrum. Figure 3.1 shows an example of the concept of adding up emission from multiple wells. The energy levels for electrons and holes in the quantum wells can be controlled in a variety of ways. The composition of the well material can be changed, thereby altering the fundamental band gap, or the width of the well can be adjusted, affecting the energy of the ground state relative to the bottom of the well. Therefore, the “deepest” wells need not necessarily have a lower band gap; if they are wider wells, the ground state will not be raised from the bottom as much by the quantum size effect. For the remainder of this thesis, the term “deeper” will be used to describe any wells with a lower ground state energy.

Large well separation (about a few tens of nm, depending on the depth of the wells) helps prevent tunneling and thermalization of the carriers in the various wells, which allows the broad spectrum to persist. Structures with multiple, different, quantum wells have been grown before for other applications[38–43], but not with GaInNAs.

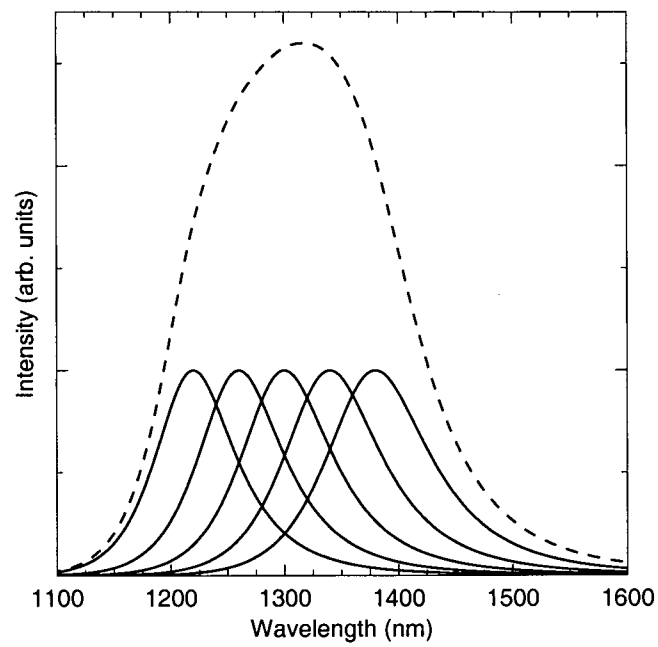


Figure 3.1: The sum of five hyperbolic secant functions (discussed in section 3.4, solid lines) combined to produced one broadband spectrum (dashed).

3.2 Using Temperature to Control Emission Spectra

The concept presented in section 3.1 and figure 3.1 is overly simplified. Unfortunately, if different quantum wells are placed in the same structure, excited electrons and holes will show a preference to recombine in a certain well. In particular, if the carriers can transfer between wells, one would expect them to accumulate in the deepest well. The emission from this well would then dominate the output, leading to a narrower spectrum than the superposition of isolated wells, which is not ideal for OCT.

One way to ameliorate the above situation is to reduce the temperature. The reduced thermal motion of carriers lowers their ability to migrate to the deepest wells. Confining carriers is easier with GaInNAs wells because they are deeper than GaInAs wells in GaAs or InP.

A simple estimate of the rate of transfer between wells can be made. A GaInNAs quantum well in a GaAs crystal, emitting photons at 1200 nm, will have a potential barrier around 0.3 eV for electrons, assuming a conduction band offset of around 80%. Given an escape attempt rate of 10^{12} Hz, the rate of thermal excitation out of the well would be $10^{12}e^{-\frac{0.3\text{eV}}{k_bT}}$ Hz. At 300 K this rate is about 10^7 Hz, which is rather close to the radiative recombination rate (around 10^8 Hz). The confinement for holes would be even worse, due to the high conduction band offset. By lowering the temperature to 100 K, the rate of thermal excitation out of the wells would drop to around 10^{-3} Hz, which is obviously much lower than the recombination rate. In this case the wells would behave independently, each emitting at its own wavelength, with

its own thermally broadened spectrum.

Temperature modulation should allow tuning of the output spectrum as required. Some communication between wells could be useful if equal pumping is not possible, and, in any event, operation at extremely low temperatures is not feasible, even if it were desirable.

Photoluminescence efficiency is improved at low temperatures, due to the reduction of non-radiative recombination rates. This has the benefit of making the target source intensity easier to achieve. Emission spectra narrow at low temperatures because thermal broadening effects are reduced. The design calls for this problem to be mitigated by the addition of more quantum wells at a fine enough wavelength spacing to keep the overall spectrum smooth. Liquid nitrogen is widely available in hospitals, making stabilized operation at around 100 K feasible for a semiconductor OCT light source.

3.3 Cladding Layers

Other layers of material besides the quantum well and GaAs are required to improve the source characteristics. For instance, the addition of AlGaAs optical cladding layers above and below the active quantum well region forms a waveguide that increases light output from the edge of the sample, since photons are guided in the plane of the well.

Another cladding procedure used recently[44–53] is the addition of thin layers of GaNAs surrounding the GaInNAs quantum well. The purpose is to reduce the potential barrier surrounding the well to lower the ground state since it depends on the barrier height. This extends the emission wavelength

without adding more nitrogen to the well, which is preferable since nitrogen can degrade photoluminescence efficiency.

Figure 3.2 shows a schematic of a double quantum well structure with GaNAs cladding. The corresponding band diagram for one of the wells is shown in figure 3.3. The conduction band offset is depicted schematically at about 80% as has been measured experimentally[54]. Figure 3.4 illustrates the changes in the ground state wavefunctions and energy levels when GaNAs cladding layers are added to a quantum well structure.

GaNAs cladding layers also affect the nature of strain in the heterostructure. GaNAs is under tensile strain when grown epitaxially on GaAs, whereas GaInNAs is compressively strained when the concentration of In is more than about three times as much as the N concentration (usually the case in our structures). The use of tensile-strained cladding allows thicker or deeper quantum wells to be grown without relaxation since the average strain is reduced.

GaInNAs cladding layers, usually lattice matched to GaAs, have also been used, with similar results[55, 56]. Although this type of cladding will not reduce the average strain, Liu proposes that the reduced strain mismatch at the interface between well and cladding improves structural properties[45]. The combination of GaInNAs and GaNAs layers around the wells has been tried as well, in a further attempt to manage strain[57].

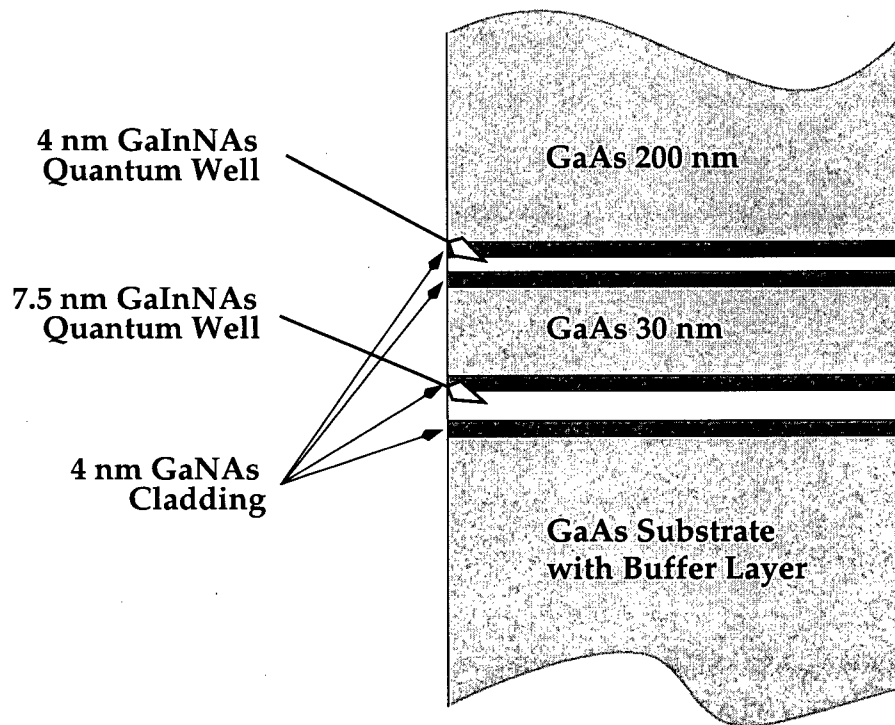


Figure 3.2: A schematic of a double quantum well structure with GaNAs cladding layers.

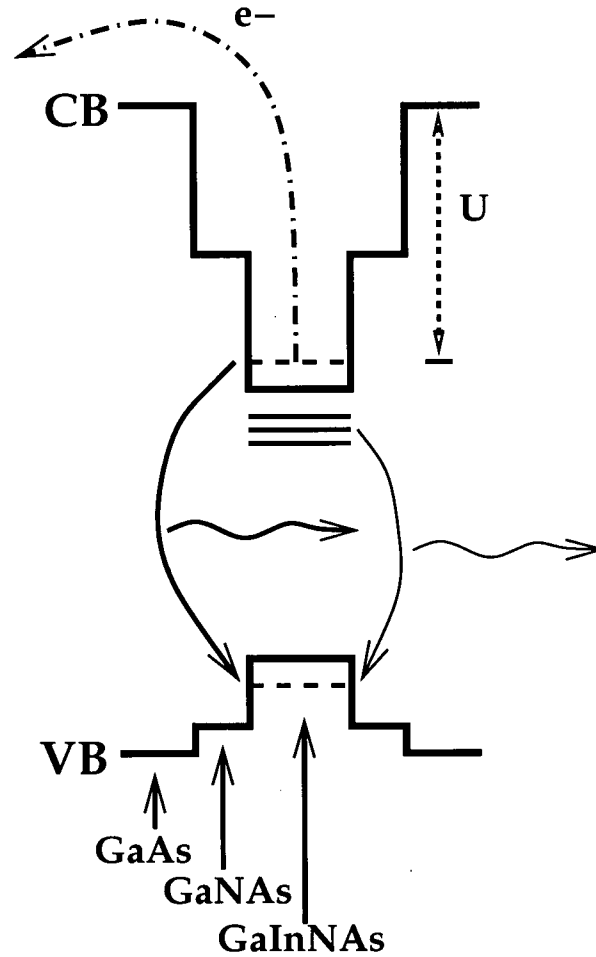


Figure 3.3: A band diagram for a quantum well with GaNAs cladding. Photon emission (wavy lines) due to recombination from the conduction band (CB) to the valence band (VB) is depicted, along with emission from in-gap cluster states. Thermal hopping of an electron out of the upper well is shown (dot-dash), overcoming an energy barrier U . The dashed lines in the wells are representative of the ground states of the finite square well.

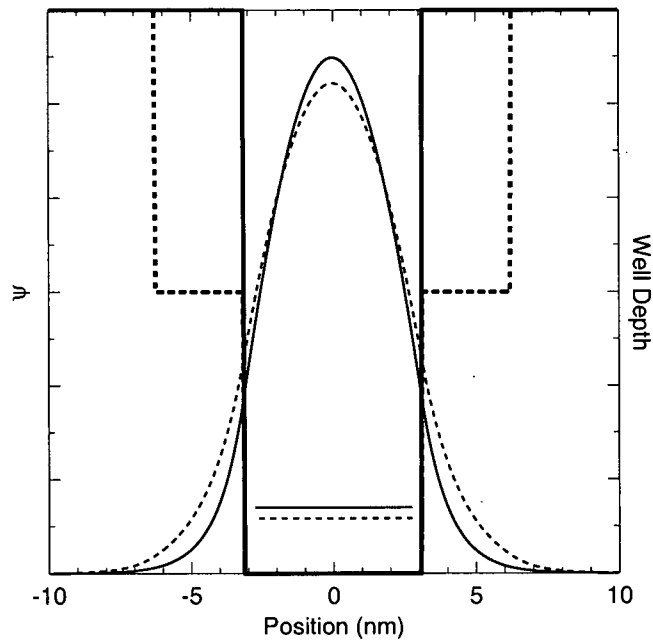


Figure 3.4: Wavefunctions (curves) and ground state energy levels (horizontal lines in the well) for the depicted well configurations with (dashed) and without (solid) GaNAs cladding layers.

3.4 Stimulated Emission

The light output of the OCT source can be increased with stimulated emission. The source design calls for optical pumping with a high power (~ 6 W) multimode stripe laser diode at 808 nm. With enough input power, the sample will enter the stimulated emission regime. The pump will be focused to a thin line ($\sim 5 \mu\text{m}$) on the sample, perpendicular to the emitting edges. Unfortunately, stimulated emission is usually accompanied by a reduction in linewidth, which is not desirable for our source. If the emission peaks from the individual quantum wells become too narrow, the spectrum will no longer be smooth. Furthermore, to suppress lasing, steps will have to be taken to prevent feedback, as in superluminescent diodes.

Possible actions to eliminate feedback include antireflection coatings on the end facets, polishing the edges at an angle to the pumping stripe, or tilting the stripe[41]. Careful control of the pump power and gain length (sample size) should allow the retention of a broadband emission spectrum while achieving increased light output.

An estimate can be made of the amount of spectral narrowing that occurs when the system undergoes stimulated emission. We assume that the gain spectrum has the same shape as the spontaneous emission spectrum. They can be modelled using a hyperbolic secant function given by

$$g(E) = \frac{A}{\cosh(\frac{E-\mu}{k_b T})}, \quad (3.1)$$

where A is a constant, E is the emission energy and μ is the peak energy. The gain of an amplifier is given by[4]

$$G(E) = e^{g(E)L}, \quad (3.2)$$

where L is the length of the gain medium. For our distributed source we need to integrate over the gain region. This takes into account the fact that light is generated throughout the pumped region and experiences different amplification depending on how far it travels in the sample. In this case the gain is

$$G(E) = \int_0^L \frac{e^{g(E)x}}{L} dx = \frac{e^{g(E)L} - 1}{g(E)L}. \quad (3.3)$$

Figure 3.5 shows examples of spectra generated using equation 3.1 and narrowed using equation 3.3 for various values of L . The plot shows $g(E)G(E)$, the spontaneous emission spectrum (assumed the same as the gain spectrum above) multiplied by the gain. The dependence of the full width at half maximum (FWHM) of the spectrum on the amount of gain is shown in figure 3.6. The narrowing is significant, but should be acceptable for use in a multiple-quantum-well OCT source, provided that the unamplified emission spectrum is tailored to take the narrowing into account.

3.5 Model for the Energy Levels in Quantum Wells

In order to predict the behaviour of the quantum wells, a theoretical model was developed for the GaInNAs structures. For a proper design, it is necessary to know the energy levels in a well, given the composition of the material and the width of the well. These calculations are complicated by inconsistencies in the values of the various material parameters for GaInNAs in the literature.

Routines were written in Python, a cross-platform scripting language, to

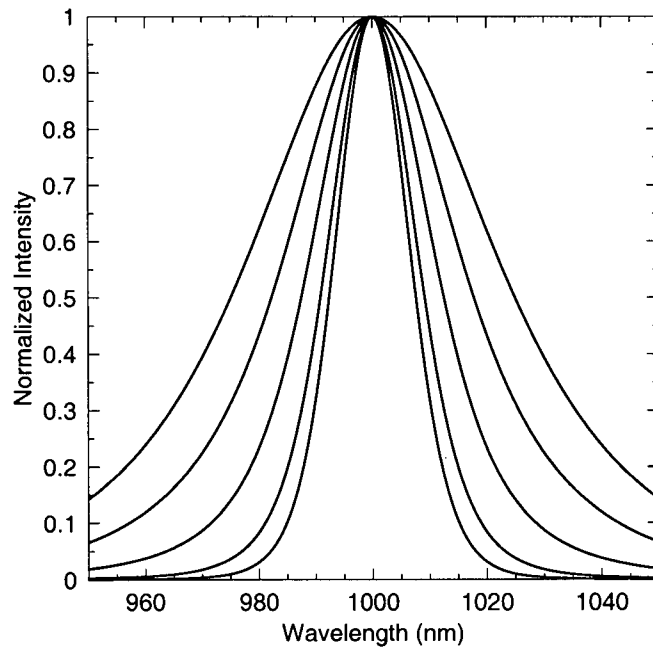


Figure 3.5: Calculated emission spectra for various levels of gain. The outer curve is unamplified. The peak gains for the inner curves are 4, 36, 658 and 9227, respectively. The maximum intensities are normalized to unity for easy comparison of the lineshapes.

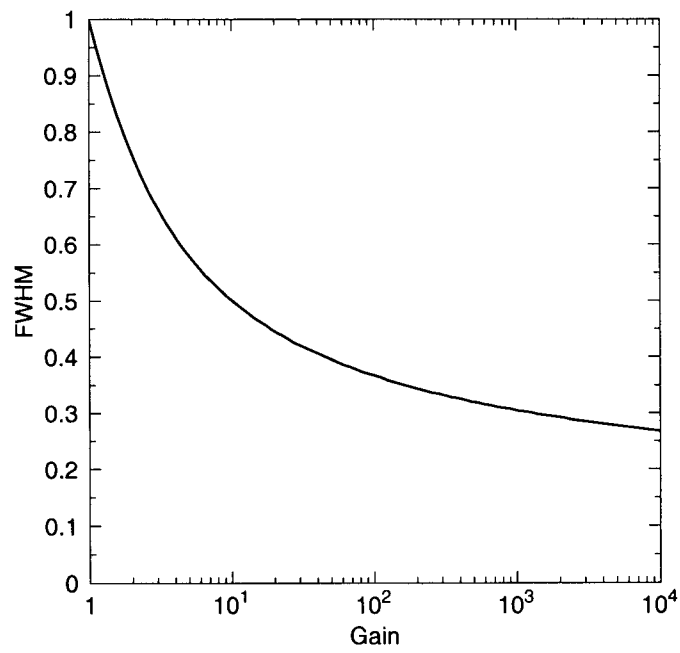


Figure 3.6: The dependence of FWHM on gain. Both axes are normalized.

calculate various quantities related to the GaInNAs system, given information available from numerous experimental and theoretical sources described below. Routines were also created to solve the finite square well problem using these parameters and to return an estimated emission wavelength.

When the quantum well material is not latticed matched to the substrate, as is the case in all of our samples, strain plays a role in modifying the band gap in the well. Here the biaxial strain is defined as

$$\varepsilon = \frac{a_{subs} - a_{well}}{a_{subs}}, \quad (3.4)$$

where a_{subs} is the lattice constant of the substrate (GaAs) and a_{well} is the lattice constant of the GaInNAs well material in bulk form. a_{well} was calculated using Vegard's law[58] and data for the binary endpoint compounds. The changes in the valence and conduction band energy levels (dE_v and dE_c , respectively) were taken to be

$$dE_c = 2a \left(\frac{C_{11} - C_{12}}{C_{11}} \right) \varepsilon, \quad (3.5a)$$

$$dE_v = b \left(\frac{C_{11} + 2C_{12}}{C_{11}} \right) \varepsilon, \quad (3.5b)$$

where a is the hydrostatic deformation potential, b is the tetragonal shear deformation potential, and C_{11} and C_{12} are the appropriate elastic constants[59–62]. The modification to the band structure varies for the conduction and valence bands due to the differences in the character of the orbitals (s in the conduction band, p for the valence band). Deformation potentials and lattice and elastic constants were obtained using linear interpolation and values from Vurgaftman's review papers[63, 64].

The GaInNAs electron effective mass was taken to be that of a GaInAs alloy with the same indium concentration, calculated by interpolation. When

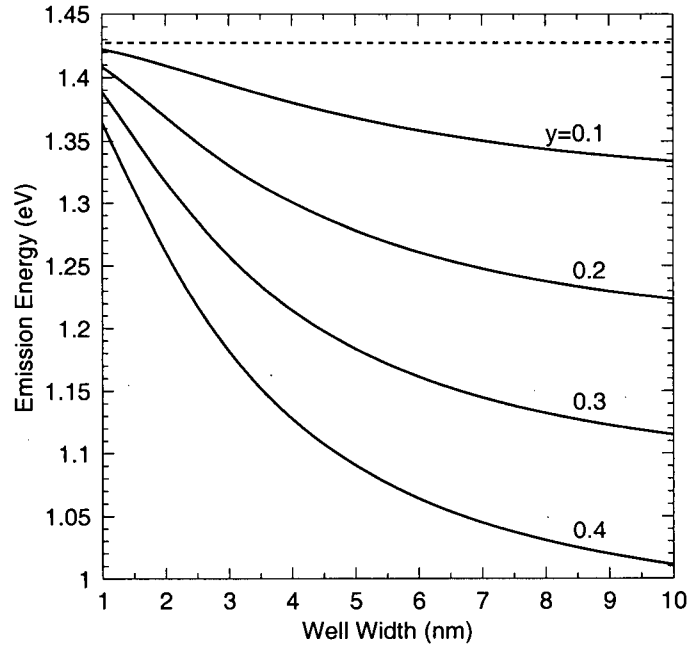


Figure 3.7: Results of the finite square well calculations for four $\text{Ga}_{1-y}\text{In}_y\text{As}$ quantum wells. Emission energies are calculated for the ground state. The solid lines correspond to indium concentrations of $y = 0.1, 0.2, 0.3$, and 0.4 , as indicated. The dashed line indicates the band gap of GaAs.

nitrogen was present in the material, the value was adjusted up by $0.03m_0$, as is suggested by Hetterich and Gass[54, 65]. The heavy-hole effective mass for GaInNAs was calculated for the [001] direction using Luttinger parameters for GaAs. Again, necessary parameters were found in Vurgaftman[63, 64]. A conduction-band offset of 0.8 was assumed, following Hetterich[54].

Figure 3.7 shows calculated emission energies for a variety of well configurations. Room temperature values for material parameters were used in all calculations.

Chapter 4

The Band Gap of Dilute Nitrides

This chapter concerns the understanding of the variation of band gap with alloy composition for the materials systems of interest. Knowledge of the band gap is a prerequisite for the design of the OCT source and many other devices. Various theoretical models are compared with available experimental data.

4.1 Band Gap Bowing

For ternary alloy semiconductors, the band gap is usually not a linear function of composition. The deviation from linearity can often be well approximated with a quadratic term. For a general ternary compound $J_xK_{1-x}L$, the band gap is given by[66]

$$E_g = xE_{JL} + (1 - x)E_{KL} + cx(1 - x), \quad (4.1)$$

where E_{JL} and E_{KL} are the band gaps for the binary compounds and c is called the bowing parameter. These bowing parameters are determined experimentally and have been compiled for a wide variety of materials. Figure

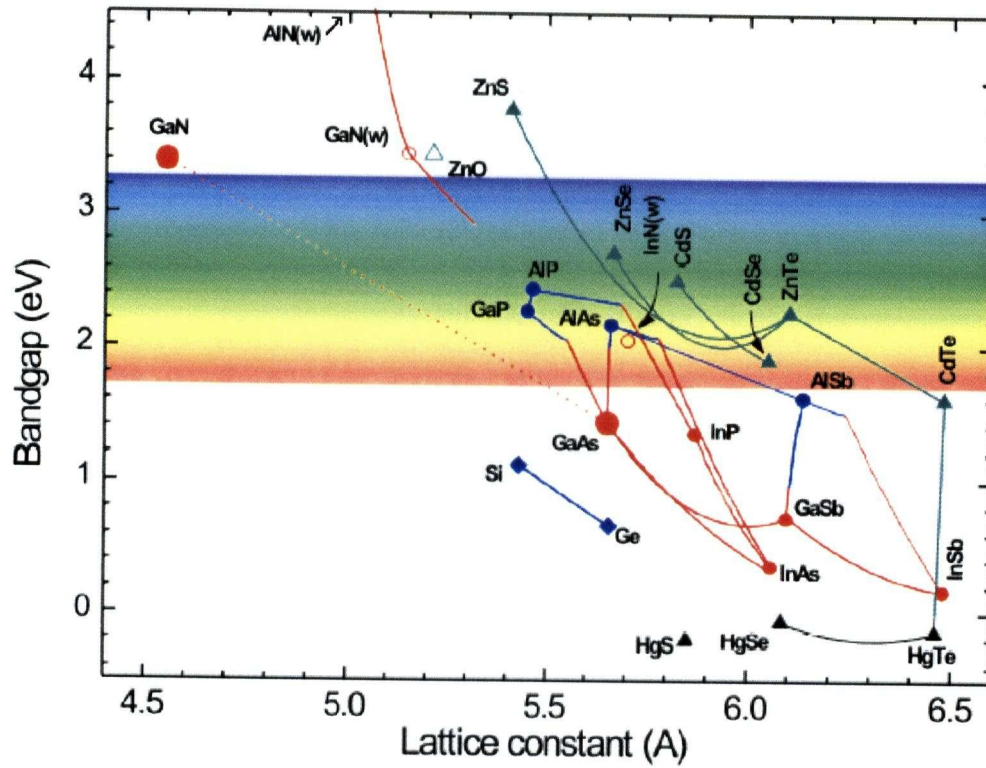


Figure 4.1: Band gap map for various semiconductor alloys[67]. Band gap bowing is evident for many ternary compounds. The dotted line between GaN and GaAs shows a linear interpolation, which is not accurate for the GaNAs alloy.

4.1 shows the variation of band gap with composition for some common semiconductors.

4.2 GaNAs

The band gap of the GaNAs alloy cannot be properly described using a standard bowing parameter model. If a linear approximation were used, the addition of nitrogen to GaAs would result in an increase in the band gap.

However, due to the bowing phenomenon, the band gap instead decreases, and does so at an enormous rate[8], more than 50 times larger than for other alloying elements. Moreover, the relation is not quadratic, ruining the bowing parameter fit. Usually a composition dependent bowing parameter is assumed and tends to fit the experimental data well, but is less elegant[8, 68]. Vurgaftman recommends the use of a band anticrossing model to determine the band gap of GaNAs[63]. Although there is some disagreement on the parameters, this approach seems to work well.

E. Nodwell developed a linear combination of atomic orbitals (LCAO) model to investigate the properties of GaNAs[25]. Results from this model have been compared with experimental data and found to be highly accurate. An sp^3s^* Hamiltonian was used, accounting for the partially filled s and p orbitals, as well as the next-highest orbital, an empty s orbital. Spin-orbit effects were neglected. Nearest-neighbour and next-nearest-neighbour overlap integrals were parameterized using Harrison's universal overlap matrix element scheme[69]. A constant factor was applied to all the overlap elements for nitrogen, to account for its small size.

Typical calculations were carried out with a $3 \times 3 \times 3$ supercell of conventional zinc-blende unit cells for a total of 216 atoms. Figure 4.2 shows a comparison of a computed density of states (DOS) from the model with experimental x-ray absorption and emission spectroscopy measurements. The variation of band gap with composition was also calculated and is shown in figure 4.3. The parameters for Ga, As, and N were initially determined by fitting to known band structures for GaAs and GaN using an iterative thermal annealing algorithm. The N $2p$ orbital energy was then adjusted to

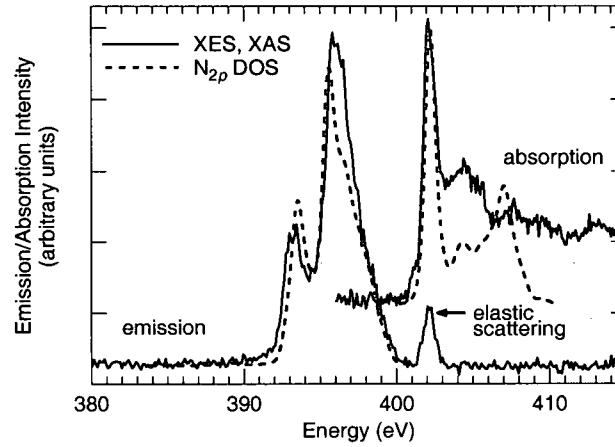


Figure 4.2: N K-edge absorption and emission spectra for a $\text{GaN}_{0.02}\text{As}_{0.98}$ sample. The energy scales for the absorption and emission spectra are aligned with the aid of the elastic peak associated with diffuse scatter in the x-ray emission spectrum. The dashed lines are the smoothed N 2p densities of states from the LCAO model. This figure was originally presented in Physical Review B, **69**:155210[25].

fit the x-ray data. The N 3s (s^*) energy was adjusted to fit the band gap of GaNAs.

4.3 GaInNAs

Due to the giant band gap bowing associated with nitrogen, the conventional methods[70] of parameterizing the band gap of quaternary dilute nitride alloys do not work. Numerous other methods are currently used to model the band gap of GaInNAs, including band anticrossing models[63, 71], density functional theory[19], LCAO models[72], and other interpolation techniques[73]. These approaches either require large numbers of parameters or are prone to inaccuracy. An easy to use system that is at least relatively

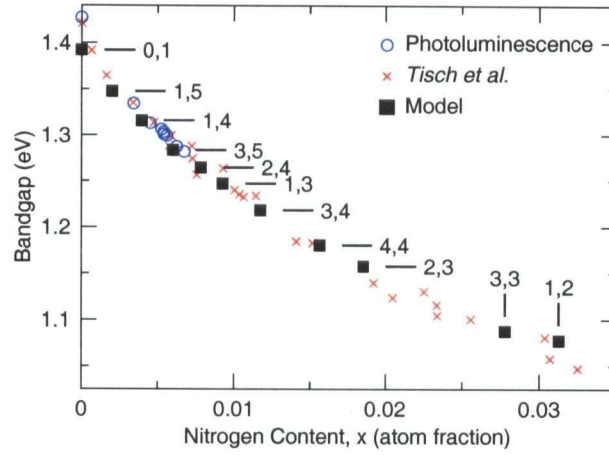


Figure 4.3: Band gap dependence on nitrogen concentration, showing the agreement between photoluminescence data from our samples, published optical data by Tisch[8], and the LCAO model. For the model points, the number of nitrogen atoms and the size of supercell are indicated (e.g., “1,3” indicates 1 nitrogen atom in a supercell of $3 \times 3 \times 3$ conventional unit cells. This figure was originally presented in Physical Review B, **69**:155210[25].

accurate is essential for device design work.

To address this problem, a new model that uses only one adjustable parameter is proposed. The form of the fit is

$$E_g(x, y) = E_g(0, 0) - F(x) - G(y) - AF(x)G(y), \quad (4.2)$$

where $E_g(0, 0)$ is the band gap of the semiconductor with no alloying elements, $F(x)$ is the known concentration dependence for one ternary compound, $G(y)$ is the dependence for the other ternary and A is an adjustable coupling parameter. The known functions ($F(x)$, $G(y)$) are the amount of band gap reduction upon the addition of specified concentration of the alloying element in question. For instance, if 10% of the Ga atoms in GaAs are replaced by In, the band gap drops by about 0.15 eV. So if $G(y)$ is for the $\text{Ga}_{1-y}\text{In}_y\text{As}$ ternary, then $G(0.1) = 0.15$ eV.

For $x = 0$ or $y = 0$, the last term in equation 4.2 is zero and the fit will match the known behaviour for either of the ternary compounds. For any fixed concentration of one element, the fit takes on the form of a constant minus the known ternary dependence (for the varied parameter) multiplied by some factor. A feature of the expression in equation 4.2 is that it maintains the same shape of concentration dependence as the ternary compound if the concentration of one of the elements is held fixed. If a third term of say xy had been used, the result would be adding a constant slope to the equation. This can cause the curvature of the band gap concentration dependence to change sign in a way not supported by experimental evidence.

In order to test the fit, a comparison was made to the experimental data on the GaInNAs system gathered by Duboz[71]. The parameter A was optimized by minimizing the sum of the squares of the deviations of the calculated

values from the published experimental data. In this case $F(x)$ was taken to be the x dependent bowing parameter fit for $\text{GaN}_x\text{As}_{1-x}$ from Tisch[8] and $G(y)$ was a standard bowing parameter model for $\text{Ga}_{1-y}\text{In}_y\text{As}$ with values from Vurgaftman[64]. This model was also used to determine the $\text{Ga}_{1-y}\text{In}_y\text{As}$ band gaps corresponding to Duboz's data (presented in the form of band gap reduction due to N).

Since the experimental data were from strained samples, the fit was adjusted to take this into account. The relations in equation 3.5 were used to correct $G(y)$ to values appropriate for strained epilayers grown on GaAs (the experimental data used for $F(x)$ was already for strained samples). A value for A of $-0.47 \pm 0.10 \text{ eV}^{-1}$ was found when the model was applied to Duboz's set of data. The negative sign means that In and N together have a smaller effect on the band gap than the sum of their individual effects. This is an important factor to consider when designing devices based on the GaInNAs system.

Figure 4.4 shows the results of the fit compared to the experimental data for $0 \leq x \leq 0.055$ and $0 \leq y \leq 0.6$. The standard deviation from the experimental values was 28 meV. This is comparable to the agreement achieved by the band anticrossing model of Duboz where the standard deviation was 21 meV. Our proposed method is not meant to take the place of band anticrossing or other theoretical models, but rather to be a convenient empirical fit for use in device design.

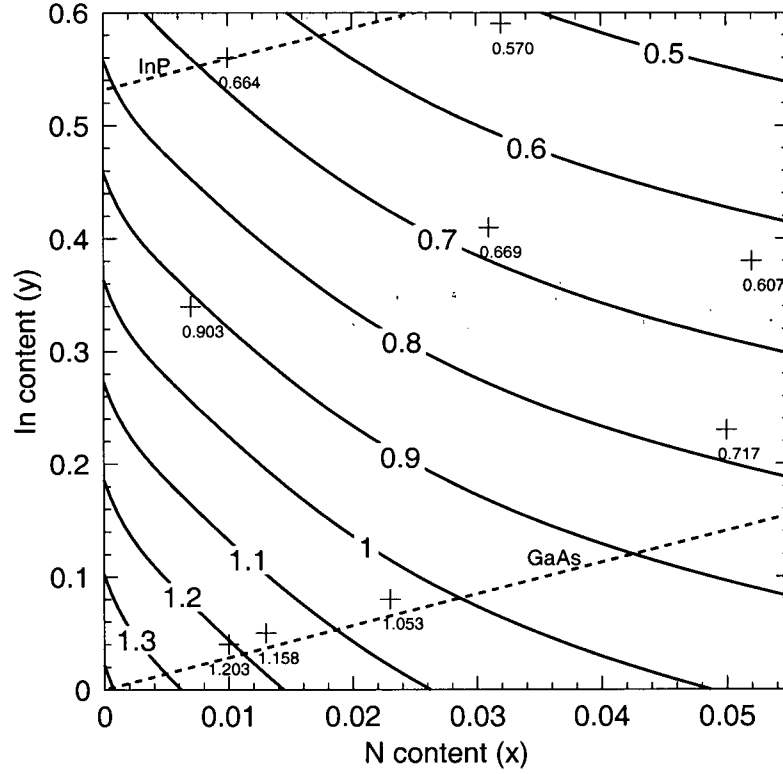


Figure 4.4: Band gap map for strained $\text{Ga}_{1-y}\text{In}_y\text{N}_x\text{As}_{1-x}$ on GaAs substrates calculated from equation 4.2 with $A = -0.47 \pm 0.10 \text{ eV}^{-1}$. Contour labels are in eV. Experimental data points (+ symbols) were gathered by Duboz[71] with labels in eV. Lattice matched conditions for GaAs and InP substrates are shown as indicated (dashed). Band gap values for material grown on InP would vary slightly due to the difference in strain.

4.4 GaNAsBi

In addition to being used as a surfactant, bismuth can be incorporated into GaAs, where it greatly reduces the band gap[74]. It has been predicted that the co-alloying of Bi and N should lead to increased solubility and improved transport properties in a way analogous to improvements seen with charge co-doping in semiconductors[75]. The large size of Bi atoms should also help counteract the effect of the small N atoms, easing coherent epitaxial growth. Bi and N co-alloying in GaAs has been investigated theoretically[76]. Recently, quaternary GaNAsBi alloys have been grown by MBE[26, 77]. As for the case of In and N, the use of Bi and N allows for growth of lattice matched layers on GaAs.

Four $\text{GaN}_x\text{As}_{1-x-y}\text{Bi}_y$ samples grown using MBE were characterized using Rutherford backscattering spectrometry[26], photoluminescence, and electroreflectance measurements. The results were fit using the one parameter model described above. The resultant band gap map is shown in figure 4.5. In this case, the parameter A was found to be $0.7 \pm 0.7 \text{ eV}^{-1}$. A linear fit (83 meV/%) to the band gap of $\text{GaAs}_{1-y}\text{Bi}_y$ [78] was used for $G(y)$. The $\text{GaN}_x\text{As}_{1-x}$ data discussed earlier[8] was retained for $F(x)$. The standard deviation from the experimental values was 47 meV.

The positive coupling parameter for the GaNAsBi alloy means that the combination of N and Bi magnifies the band gap reduction compared to the sum of their individual effects (although our accuracy is only marginally adequate to determine the sign of the parameter). This gives the possibility of growing low band gap semiconductors that are lattice matched to GaAs with relatively low concentrations of N and Bi. The sign of the coupling

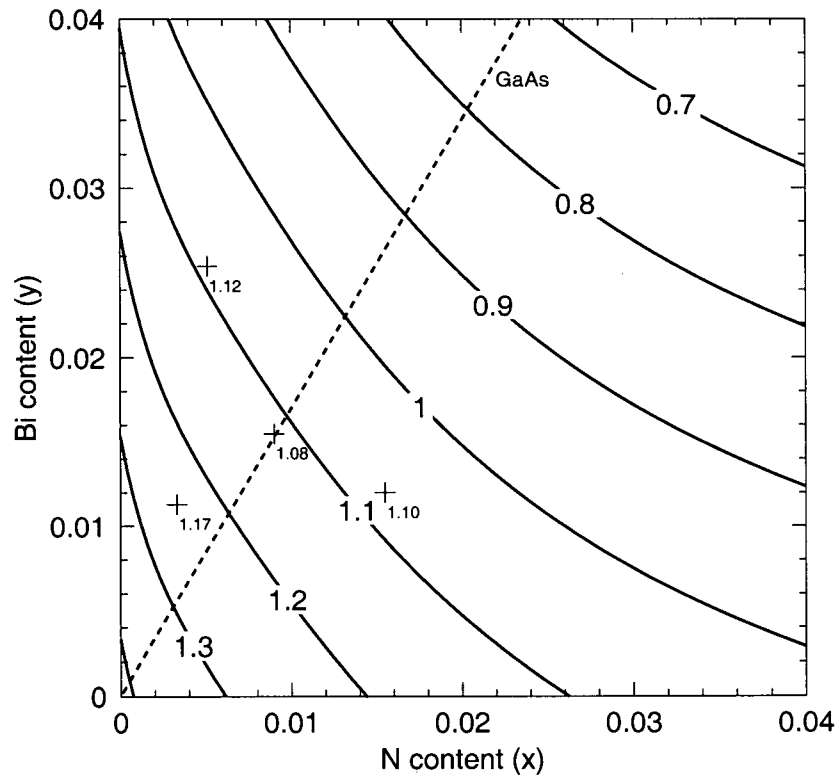


Figure 4.5: Band gap map for strained $\text{GaN}_x\text{As}_{1-x-y}\text{Bi}_y$ on GaAs substrates using equation 4.2 with $A=0.7\pm0.7\text{ eV}^{-1}$. Contours and experimental data point labels (+ symbols) are in eV. The lattice matched condition for GaAs is shown (dashed).

parameter was predicted by Janotti[76], although the value determined from our data indicates a larger interaction than was estimated. Direct numerical comparison of the coupling parameter is difficult due to the different models used. For one of our samples with 0.7% N and 1.47% Bi, Janotti's model predicts a 0 K band gap of 1.38 eV. The one parameter fit used here gives a result of 1.16 eV at 300 K. The temperature difference will account for part of the discrepancy between the two values.

Chapter 5

Photoluminescence Results

5.1 Growth Parameters

Quantum well samples for the OCT project were grown in a Vacuum Generators V80H MBE system, with conventional Knudsen effusion cells for Ga, In, and Bi, a two-zone cracker source for As₂, and a helical radio frequency plasma source for nitrogen[79]. The plasma source starts spontaneously, allowing easy modulation of the nitrogen flux, and is equipped with a baffle to reduce the effects of ions. Ultra high purity N₂ (99.999%) was fed into the plasma source via a leak valve in a gas system that was differentially pumped with a turbopump. The plasma source was operated at 150-200 MHz with a net power between 90 and 190 W with a background nitrogen pressure in the chamber in the 10⁻⁶ mbar range during growth. An As overpressure was maintained during growth, with a V/III ratio between 5 and 8. The substrate temperature during the growth of quantum well layers was 450°C, as monitored by optical band gap thermometry[12]. The Ga cell temperature was adjusted to maintain a growth rate of 0.5-1 $\mu\text{m/hr}$.

GaAs substrates with (001) orientation were outgassed in the chamber and were heated to above 600°C briefly to remove their surface oxide layer. Crystal quality and growth rate were monitored *in situ* by reflection high en-

ergy electron diffraction (RHEED), and with high resolution x-ray diffraction after growth. Despite the advantages of using Bi as a surfactant mentioned in section 2.1, it was not used here. AlGaAs cladding layers were also not generally used in order to simplify the growth procedure. All structures consisted of a GaAs buffer layer grown directly on the substrate (~ 300 nm), the quantum well region, and a GaAs capping layer (~ 150 nm). Samples were not annealed for this work, but the possible improvement in PL efficiency could prove useful for future devices.

5.2 Description of Samples

Table 5.1 shows the characteristics of the samples grown for this work (with the aid of E.C. Young, N.R. Zangenberg, E. Nodwell, M.B. Whitwick and S. Tixier). The values in the table were determined through a combination of x-ray diffraction measurements, photoluminescence data, and the quantum well model.

Sample number 1168 is a single GaInAs quantum well, whereas 1183 is a single GaInNAs well. 1150 is a single GaInAs well with AlGaAs cladding layers. These samples provide a baseline for comparison with the multiple-quantum-well samples.

Samples 1437 and 1438 were intended to be double quantum well structures with different In contents to change the emission energy of the two wells. The well positions were reversed between samples, with 1437 having the deep well grown first. Unfortunately, during the growth of 1437, the nitrogen plasma failed to ignite for the first well, causing a nitrogen-free

GaInAs well to be grown. It was decided to bury the well with approximately 500 nm of GaAs and then restart the growth recipe. The accidental GaInAs well does not seem to have been successfully removed from the PL spectra however, as discussed below.

Growing quantum wells of different compositions in the same sample requires adjusting the In effusion cell temperature during the growth of the GaAs spacer layers. If an interruption in the growth is to be avoided, there is a limit to the range of possible well compositions and a minimum width of the spacer layer because it takes time for the cell to stabilize. It is also preferable to not have to adjust the nitrogen plasma conditions during the growth. For these reasons, the In and N compositions in the wells were kept constant for the remaining growths, while only the widths of the wells were varied. Well thickness is far easier to control than concentration and still allows adjustment of the ground state energy of the quantum well.

Runs 1483 and 1484 were double quantum well samples with the same well positions. A GaNAs cladding layer was used for sample 1484, while 1483 had no cladding. X-ray and PL data show that only 0.18% N incorporated into the well layers. This was significantly less than intended (1.5%), however the N concentration in the cladding for 1484 was 0.94%. The growth rate was significantly lower outside the well regions since there was no In flux. This is likely the cause of the increased nitrogen incorporation in the cladding layers.

Runs 1487 and 1488 were triple-well samples with well thicknesses designed to produce equally spaced emission peaks. The well orders were the same, but 1488 was to have increased levels of N and In. X-ray and PL data show that the concentration changes were minimal. The N concentration

was increased from 0.2% to 0.25% and there was only a marginal increase in In concentration. These samples had relatively small separations between wells of about 30 nm. The spacing was lowered so that the pumping would be more uniform across the wells. Although previously the spacing had been higher to ensure the elimination of tunneling between wells, 30 nm seems to be sufficient for this purpose.

Five other samples were grown in addition to those mentioned above. These samples are described in table 5.1, but were not as thoroughly analyzed for a variety of reasons. Samples 1401, 1408 and 1409 had PL emission at energies very close to the band gap of GaAs due to low In incorporation. This made their spectra hard to interpret, since emission and absorption from the substrate and GaAs epilayers affected the measurement. Samples 1464 and 1465 were accidentally grown with too high of an In concentration, causing the structures to relax due to excessive strain. The dislocations formed during the relaxation process drastically increase non-radiative recombination, virtually eliminating PL.

Table 5.1: Quantum well sample information. Values are from a combination of x-ray diffraction and PL data, as well as theoretical modelling. Entries are in order of growth (e.g. 8.8,8.5 in the widths column indicates a 8.8 nm well grown before a 8.5 nm well).

Sample Log #	N Conc. x	In Conc. y	Widths (nm)	Spacing (nm)	Comments
1150	0	0.23	5.6	N/A	single well, AlGaAs cladding
1168	0	0.33	7.8	N/A	single well
1183	0.0080	0.28	7.5	N/A	single well
1401	0	0.16,0.05	6	60	confusing PL spectrum
1408	0	0.035,0.25	7.9,6.4	89	weak PL
1409	0	0.25,0.035	6.4,7.9	89	weak PL
1437	0,0.0040 \times 2	0.26 \times 2,0.13	8.5 \times 2,8.8	\sim 500,91	see text
1438	0.0040	0.13, 0.26	8.8,8.5	91	double well
1464	0.005	0.43	6,11	50	relaxed
1465	0.005	0.43	6,11	50	relaxed
1483	0.0018	0.35	8.4,4.6	31	double well, no cladding
1484	0.0018	0.35	8.4,4.6	31	4 nm, 0.94% N GaNAs cladding
1487	0.0020	0.38	7.9,6.0,4.4	29	triple well
1488	0.0025	0.38	7.8,5.5,4.1	31	triple well

5.3 Surface Oxidation

Tests were performed on GaInAs quantum well samples to determine how surface oxidation affects photoluminescence and to establish a standard surface condition for performing measurements. The relative magnitude of surface and bulk recombination processes is important for device design and sample comparison.

An ultraviolet (UV) lamp in a metal box was used to oxidize samples with and without AlGaAs cladding layers. Ozone (O_3) was created by the UV lamp and caused oxidation at much faster rates than normal atmosphere. Single quantum well structures 1168 (no cladding) and 1150 (10 nm AlGaAs cladding) were used for these tests.

Samples were initially etched in concentrated HCl for 5 minutes to remove any oxide present. The samples were then placed into the ozone box for varying time periods and the photoluminescence intensity was measured. Figure 5.1 shows the reduction in PL intensity with increasing oxidation time. The samples labelled “cumulative” were periodically removed from the ozone box for measurements. “Etched each time” indicates that the sample was placed in the ozone box for the amount of time corresponding to the data point, removed and measured, then etched again before the next round of oxidation. The difference in results between these techniques was small, and could be due to the fact that the ozone likely takes some time to build up in the box, reducing the effect of short oxidation runs.

As can be seen in figure 5.1, the sample with cladding does not appear to have been significantly affected by oxidation, as expected. The layers of AlGaAs between the surface and quantum well seem to eliminate the

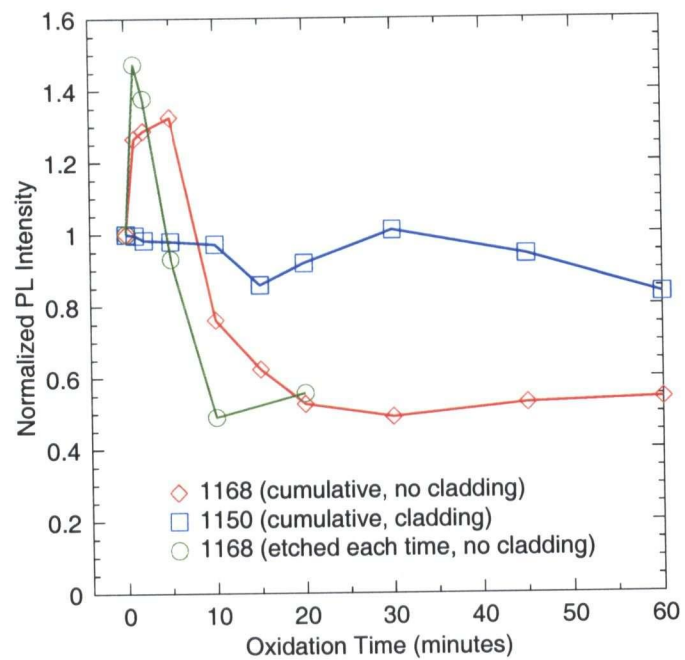


Figure 5.1: Effect of oxidation on PL intensity (normalized for comparison) for samples with and without AlGaAs cladding layers.

effect of surface recombination on photoluminescence. The unclad sample initially increased in PL intensity (by about 35%) with a small amount of oxidation. This was followed by an approximately exponential decrease in intensity (down to about 55% of the initial value) with further oxidation. Performing PL measurements before and after etching on samples that had been stored for several years showed similar changes in PL spectra. This leads us to believe that samples stored in air slowly develop oxide layers similar to those generated rapidly in the ozone box.

The initial increase in intensity is an interesting effect. Our interpretation is as follows. Dangling bonds on the GaAs (001) surface produce states in the band gap that act as efficient non-radiative recombination centres. A small exposure to oxygen passivates these bonds, which in turn reduces the recombination and increases PL intensity. After the initial passivation, oxygen migrates into the crystal and preferentially oxidizes Ga. This creates dangling bonds on As atoms, which increases non-radiative recombination, and thus reduces PL. Metallic As could form below the surface, which would cause even more non-radiative recombination.

Oxidation seems to affect only the peak height and not spectrum shape or centre wavelength, as seen in figure 5.2. This makes etching before PL measurements important if absolute intensities are to be compared, but less relevant if only emission energies or shapes are important. In general, samples measured for this work were not etched before each PL experiment. It was easier to store compared samples under identical conditions.

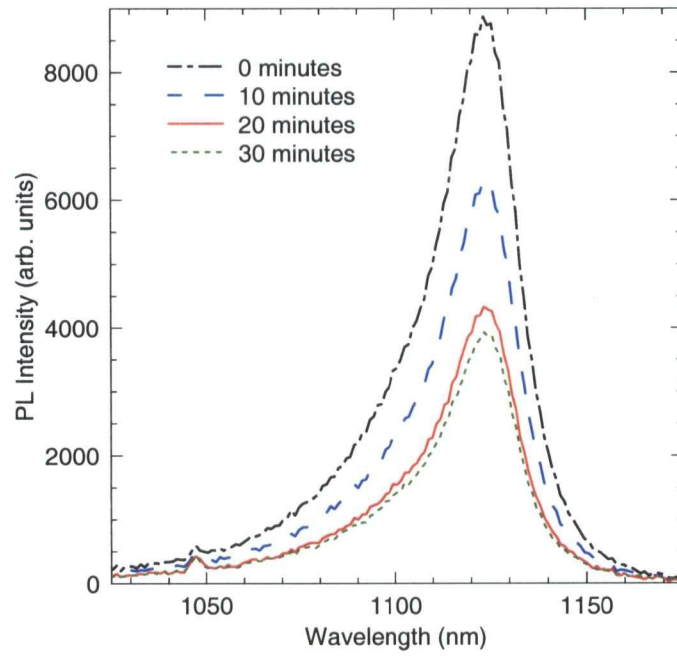


Figure 5.2: PL spectra for a GaInAs quantum well sample with no cladding (1168) for different oxidation times. Only the absolute intensity is affected.

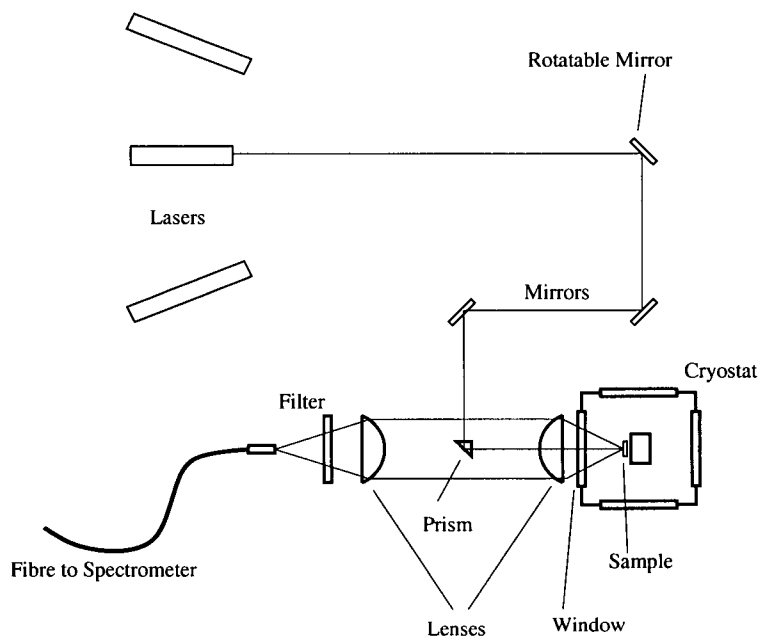


Figure 5.3: Photoluminescence measurement setup.

5.4 Experimental Procedure

Photoluminescence measurements were performed with samples in a closed cycle helium cryostat to allow measurements at temperatures between 20 and 300 K[29]. Optical access to the samples was provided by a quartz window and laser light was focused onto the sample through the same lens that collected the PL emission. A small prism was used to guide the beam between a pair of 50.4 mm diameter plano-convex lenses. Figure 5.3 shows the experimental configuration.

Different lasers were selected by turning a rotatable mirror holder to one of a set of discrete positions, each aligned for a particular laser. This allowed

the pair of mirrors that steered the beam into the prism to remain fixed for all measurements. The lens nearest the chamber was positioned one focal length away from the sample, in order to collimate emitted PL. This meant that the already collimated laser beam passing through the same lens from the other direction was focused onto the sample. The second lens focused the PL emission (collimated by the first lens) into a fibre bundle for transport to the spectrometer, where the light passed through a $50\text{ }\mu\text{m}$ slit. A longpass filter was placed in front of the fibre to block light from the pump lasers, ensuring that only PL was analyzed. The size of the prism was minimized ($<1\text{ cm}$) to reduce blocking of the PL and the fibre was positioned using an XYZ stage to maximize throughput. Emitted light was analyzed using an Acton Spectra Pro 300i spectrometer, with a liquid nitrogen cooled GaInAs array detector operated at -100°C . A grating with 150 lines/mm and correspondingly large wavelength range ($\sim 500\text{ nm}$) was used.

A variety of pumps were used to excite the samples, including a pulsed source consisting of a Nd:YLF laser with a frequency doubler, emitting 1000 pulses per second at 523 nm. The pulses had widths of about 20 ns and energies of $2.0\text{ }\mu\text{J}$. The 488 nm line of an Ar^+ laser and an 800 nm diode pump were used for high intensity continuous wave (CW) pumping. Each laser provided different information about the samples because of their varied characteristics. The pulsed source had much higher photon densities, but on much shorter timescales than the CW lasers. Longer wavelength light penetrates further into the sample because the absorption coefficient is wavelength dependent. The power and energy values given here and below for the lasers do not take into account losses in the optical system, which are

estimated at around 50%. Assuming 40% reflection from the sample face gives a net absorbed power of 30% of the stated values.

The spectral throughput of the spectrometer was calibrated by placing a 100 W tungsten-halogen lamp near the sample holder, which was then covered with a diffusely reflecting white sheet (three layers of Tyvek® were used to provide around 95% reflectance[80]). The spectrum collected by the optical system was measured using the spectrometer and recorded for a variety of grating positions and slit sizes. The light bulb can be considered to be an ideal blackbody at 3200 K so the spectra were compared to the equation

$$N(\lambda, T)d\lambda = \frac{8\pi d\lambda}{\lambda^4 \left(e^{\frac{hc}{\lambda k_b T}} - 1 \right)}, \quad (5.1)$$

where $N(\lambda, T)$ is the photon density of a blackbody for a given temperature[81]. Figure 5.4 shows a comparison of the detector measurements to the blackbody spectrum. The response dies off above 1600 nm and below 900 nm, as expected, due to the band gaps of the $\text{Ga}_{0.47}\text{In}_{0.53}\text{As}$ detector and the InP capping layer, respectively (both at -100°C). The slit size did not affect the measurements. Corrections were determined by dividing the collected data by the expected blackbody curve and applied to all PL spectra.

5.5 Photoluminescence Data

Figure 5.5 shows photoluminescence spectra from a single GaInAs quantum well sample (1168) at a variety of temperatures, excited with the CW Ar^+ laser. Figure 5.6 shows PL data from the same sample, using the pulsed laser for excitation. The high carrier concentrations created by the pulses

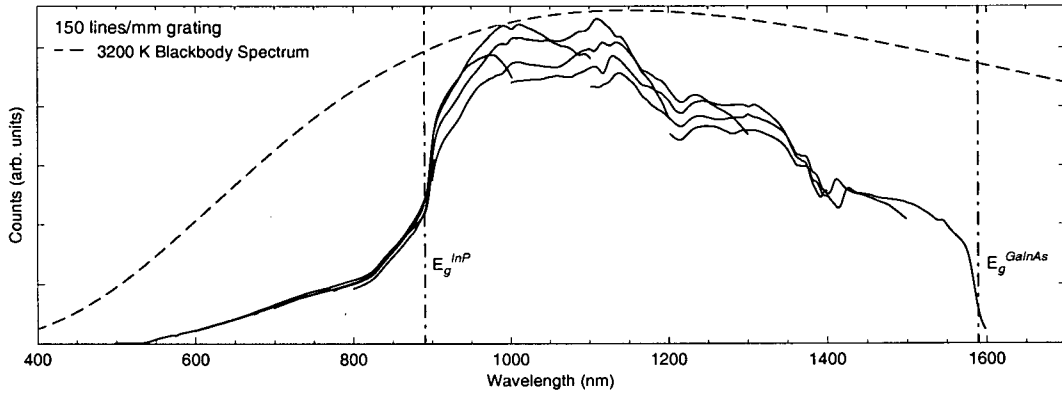


Figure 5.4: Throughput measurements for the photoluminescence setup. The eight solid lines (overlapping) are spectrometer measurements of a tungsten-halogen bulb with the 150 lines/mm grating. Each line corresponds to a different grating position, which in turn corresponds to a different measured wavelength interval (~ 500 nm per position). The dashed line is the spectrum of an ideal blackbody at 3200 K, according to equation 5.1 (scaled for comparison). The dot-dashed lines show the band gaps for the InP cap layer and GaInAs detector at -100°C , as indicated.

result in higher energy (lower wavelength) emission, and the appearance of a second peak from the next electron level in the quantum well (the e2-hh1 transition). The PL intensity increases dramatically at low temperatures for both excitation types and the emission wavelengths decrease as expected from the temperature induced change in band gap. Comparisons of integrated room temperature PL intensity from sample 1168 with spectra collected from known laser beams show quantum efficiencies of around 0.2-0.4%. These values do not take into account light trapping associated with the high index of refraction of the semiconductor material. In principle, the internal quantum efficiencies could be as much as $4n^2$ (46 times) larger.

Figures 5.7 and 5.8 show PL spectra from sample 1183, a single GaInNAs quantum well structure. The emission wavelengths are longer than for 1168, and the second level peak is not visible in the pulsed spectra. The peaks are broader and less intense, due to the nitrogen. The intensity increase at low temperatures is weaker, possibly because the wells are deeper and provide better carrier confinement. Figure 5.9 shows PL data from sample 1183 on an energy scale. The high energy slopes of the peaks show good agreement with theoretical Boltzmann distributions as indicated in the figure. Also shown is the expected low energy slope due to the Urbach edge, as given in equation 2.2. In both cases, agreement with the experimental data is lost at temperatures below around 100 K, as other factors, such as inhomogeneities in the sample, start to limit the slope.

Sample 1438 was the first double quantum well structure with strong PL. Figure 5.10 shows the temperature dependence of the emission, which consists of two widely separated peaks. The weaker peak is from the shallow

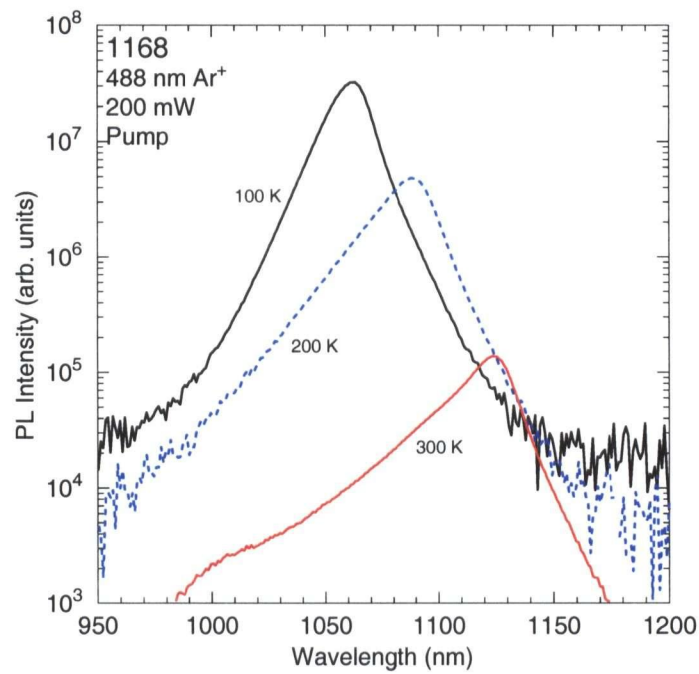


Figure 5.5: Photoluminescence spectra from a single GaInAs quantum well (1168) at a variety of temperatures. Excitation was from the 488 nm line of an Ar⁺ laser operated at 200 mW. Alternating solid and dashed lines are used for clarity.

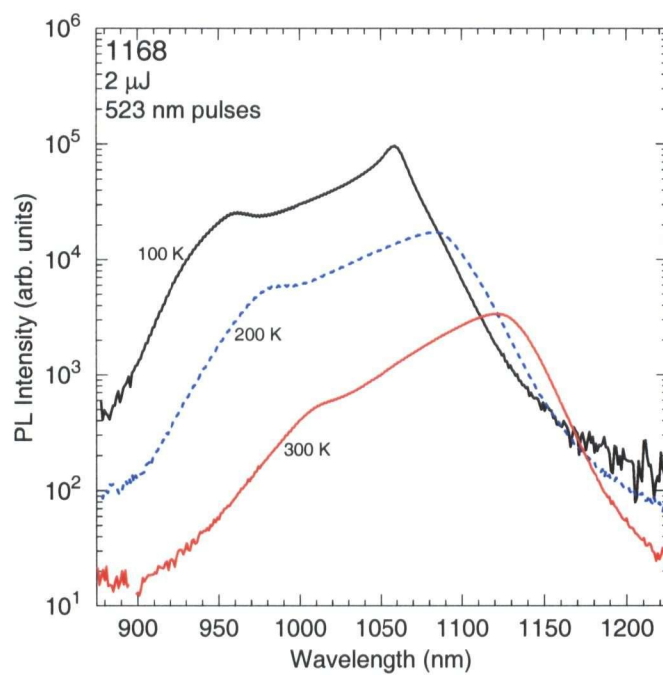


Figure 5.6: Pulsed photoluminescence spectra from sample 1168. The 523 nm source provided 1000 2 μ J pulses per second.

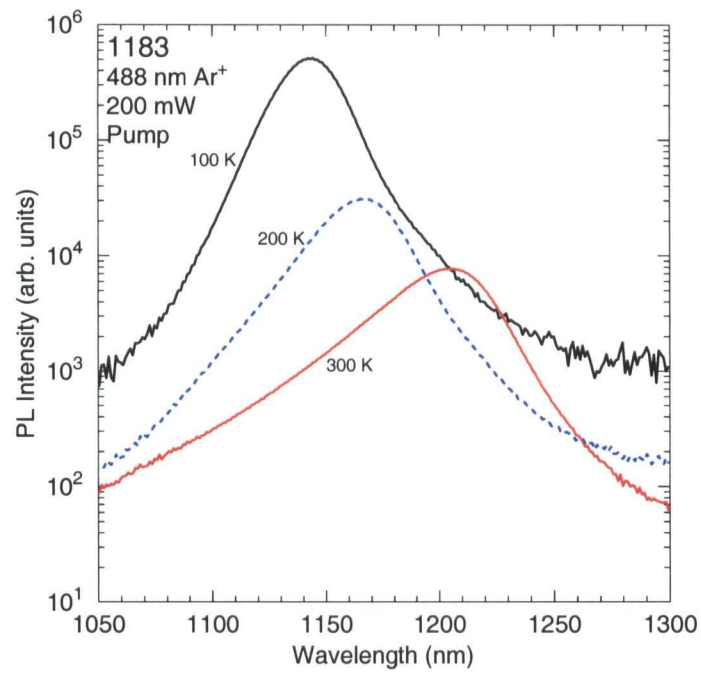


Figure 5.7: PL spectra from a single GaInNAs quantum well (1183). 200 mW, 488 nm CW excitation.

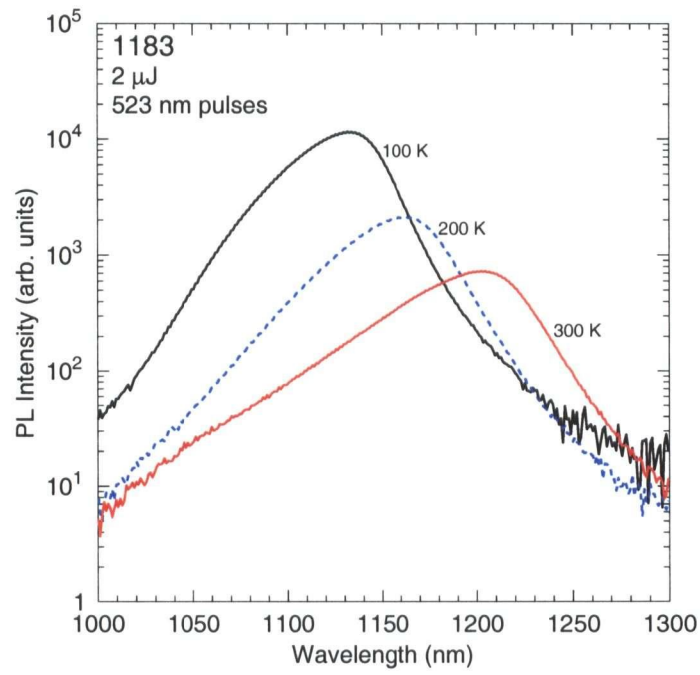


Figure 5.8: Pulsed PL spectra from sample 1183. Excitation was 1000 2 μ J pulses per second.

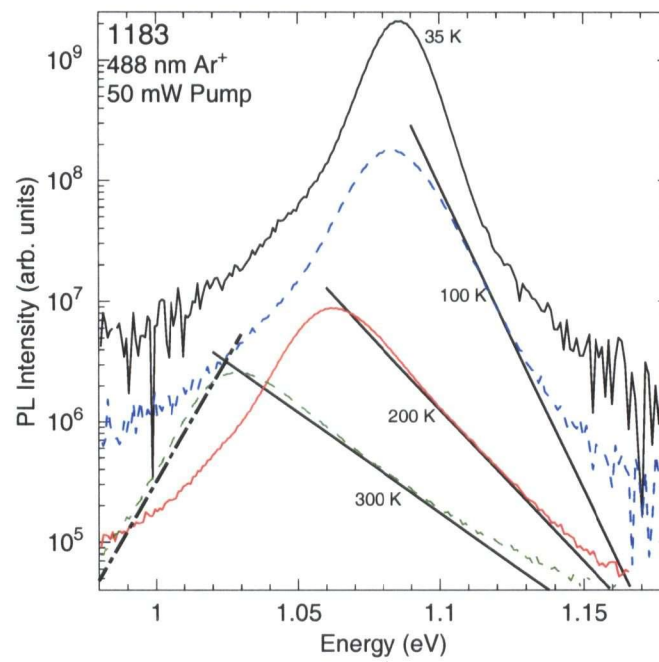


Figure 5.9: PL spectra from sample 1183 on an energy scale. The solid straight lines show Boltzmann distributions for various temperatures. Agreement is good except at very low temperatures. The dot-dashed line shows the low energy Urbach edge at 300 K.

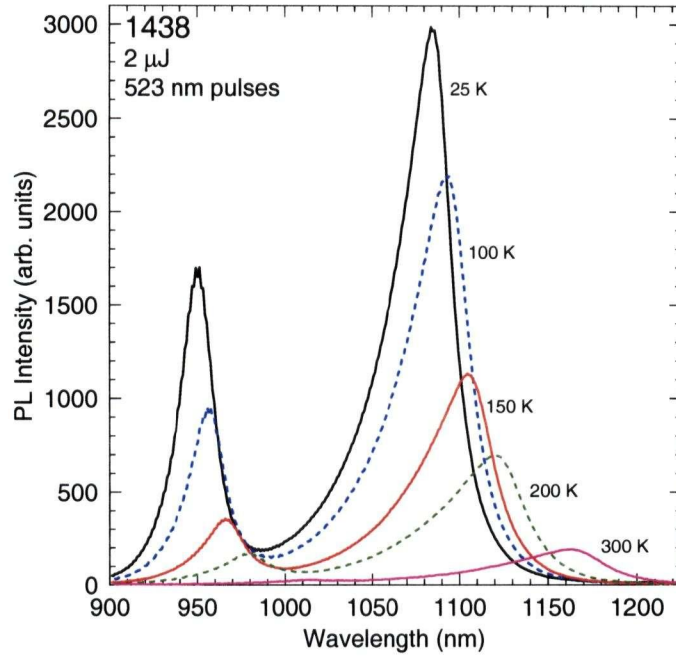


Figure 5.10: Temperature dependent PL from sample 1438, with two GaInNAs quantum wells. 523 nm pulsed excitation (1 kHz, 2 μ J).

well, which was grown first in this sample, meaning that it was further from the surface and the incident pump light. The relative intensity of the peaks changes with temperature, as expected. PL from sample 1437, which was intended to have the same two wells in reversed positions, but ended up with three wells, is shown in figure 5.11. The peak from the shallow well is strongest in this data, corresponding to its location near the surface. It is believed that the centre peak corresponds to the accidentally grown GaInAs well that was deeply buried in the structure. The longest wavelength peak disappears at higher temperatures, for reasons that remain unclear.

Photoluminescence data from samples 1483 and 1484 are shown in figures 5.12 and 5.13. GaNAs cladding layers were used in 1484, in which the deeper

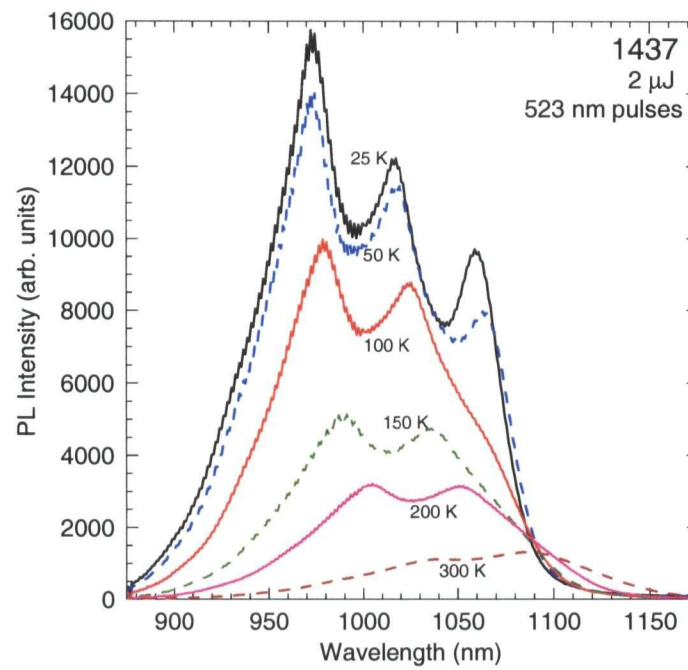


Figure 5.11: Temperature dependent PL from sample 1437, with two GaInNAs quantum wells and one GaInAs well. 523 nm pulsed excitation (1 kHz, 2 μ J).

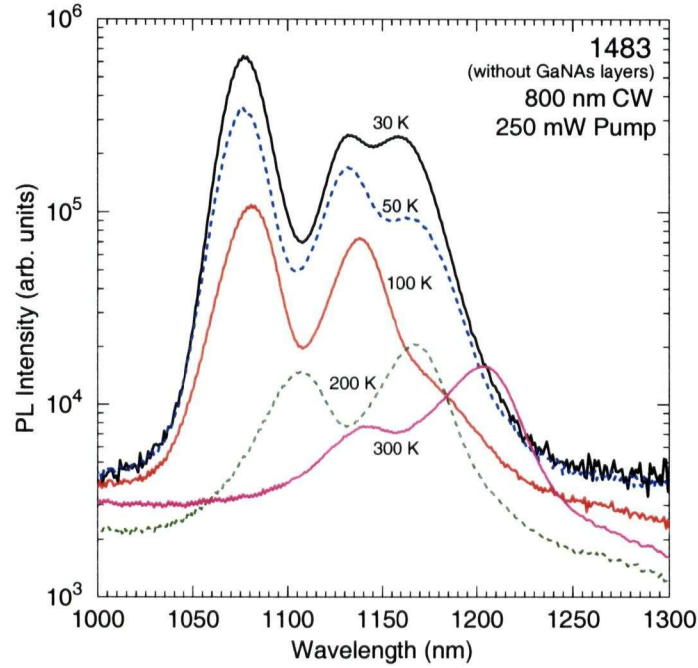


Figure 5.12: Temperature dependent PL from sample 1483, with two unclad GaInNAs quantum wells. 250 mW, 800 nm CW excitation.

well was grown first. 1483 had no cladding and the well positions were reversed. At low temperatures, three individual peaks are visible despite the fact that there are only two wells in these samples. The third peaks are attributed to emission from nitrogen cluster states in the band gap. This will be discussed in more detail in section 6.3. The emission from the wells in sample 1484 is at slightly longer wavelengths than in sample 1483 due to the effects of the GaNAs cladding on the quantum well states.

PL from the triple quantum well samples, 1487 and 1488, is shown in figures 5.14 and 5.15. Each of these samples contains three GaInNAs quantum wells grown in the same order, from deepest to shallowest. Three peaks are

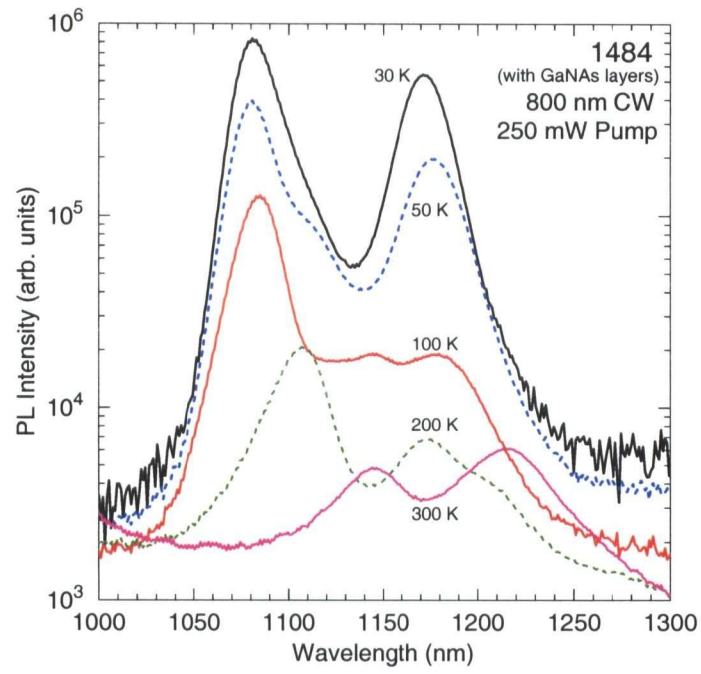


Figure 5.13: Temperature dependent PL from sample 1484, with two GaInNAs quantum wells and GaNAs cladding layers. 250 mW, 800 nm CW excitation.

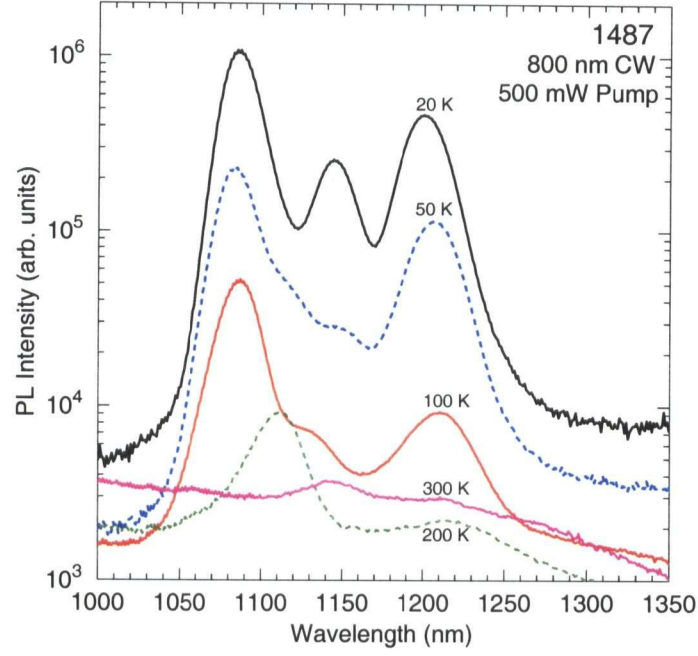


Figure 5.14: Temperature dependent PL from sample 1487, with three GaInNAs quantum wells. 500 mW, 800 nm CW excitation.

visible in the PL spectra for both samples, at slightly longer wavelengths for sample 1488, due to additional nitrogen incorporation. These results will be discussed further in the following chapter.

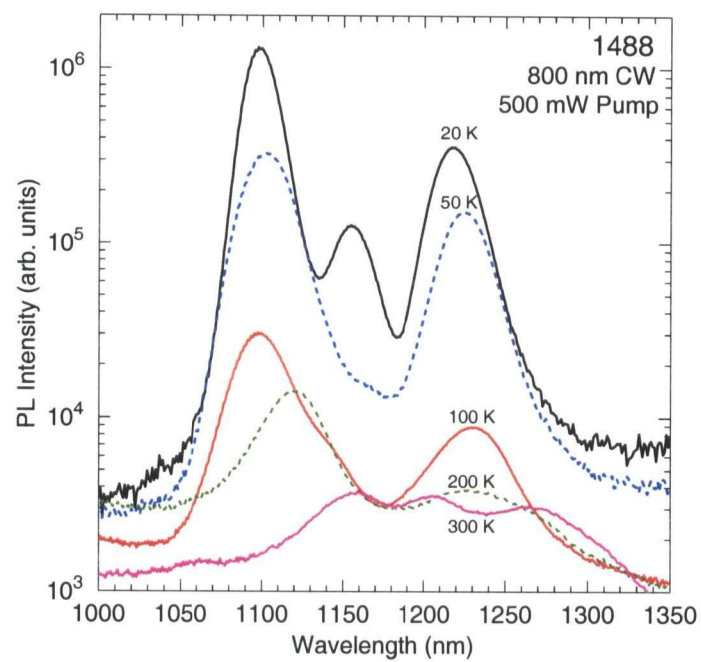


Figure 5.15: Temperature dependent PL from sample 1488, with three GaInNAs quantum wells. 500 mW, 800 nm CW excitation.

Chapter 6

Interpretation of Photoluminescence

6.1 Successful Broadband Emission

The multiple-quantum-well samples show several distinct emission peaks in the photoluminescence spectra. Figure 6.1 shows PL data from single, double, and triple quantum well samples (1183, 1484 and 1487), illustrating that broadband emission can be obtained by combining different individual wells. Unfortunately the weakest peak in the triple well case has an intensity of only about 15% of that of the strongest peak. The relative peak heights are determined by a number of competing factors, including pumping differences and thermal transfer between wells. Room temperature emission from sample 1488 has a much more uniform shape, but a correspondingly smaller intensity, as was shown in figure 5.15. This sample has a FWHM of 195 nm, which is much wider than current OCT sources, demonstrating the potential of this design.

The quantum well widths used in these samples were chosen using the calculations discussed in section 3.5 so that the corresponding emission wavelengths would be widely spaced. This was done to ease the process of identify-

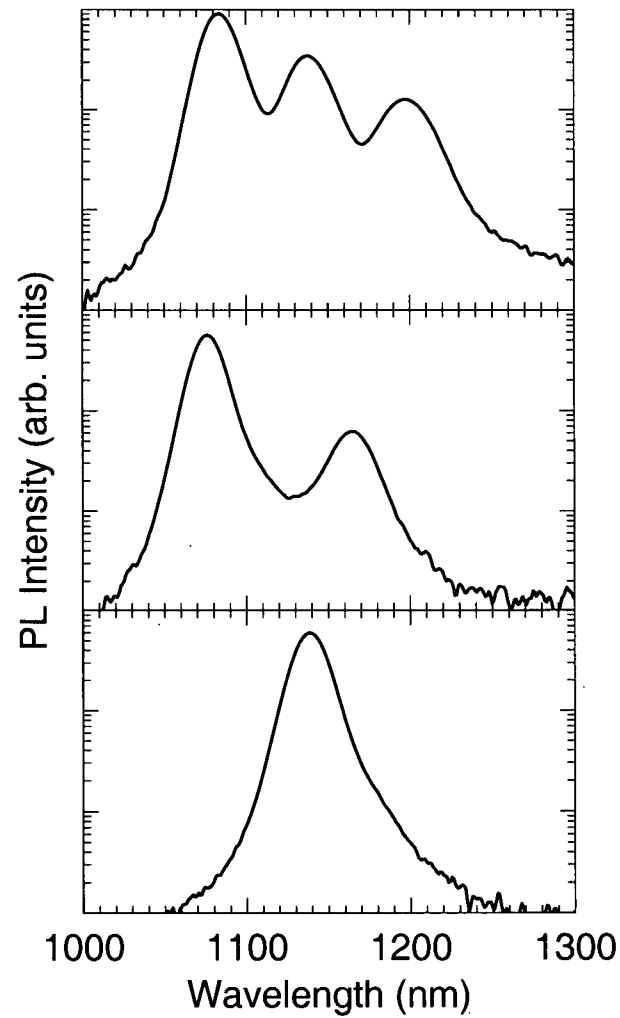


Figure 6.1: Photoluminescence spectra from samples 1183 (bottom), 1484 (middle) and 1487 (top); single, double and triple quantum wells, respectively. The sample temperature was 25 K, with 488 nm CW excitation. The panels illustrate the process of adding emission from different quantum wells.

ing the specific quantum well responsible for each peak. For the final device design, the emission wavelengths will be more finely spaced to produce a smoother spectrum. The wells need not be evenly spaced with respect to their emission wavelengths. The distribution of well widths can be adjusted to help balance the output spectra.

The choice of excitation source affects the shape of the emission spectra. For example, the top curve from figure 6.1, excited by the 488 nm CW source, can be compared with the spectra in figure 5.14, where the excitation was with the 800 nm CW diode laser. The long wavelength peak is stronger than the other two peaks in figure 5.14. This could be due to the deeper penetration of the 800 nm laser since the wide well was grown first in this sample. However, one would then expect the height of the centre peak to also be increased relative to the short wavelength peak, which is not observed. The 800 nm pump in the OCT source design should provide an advantage due to lower absorption in GaAs at longer wavelengths.

6.2 Temperature Dependence of Emission

Photoluminescence intensity is greatly increased at low temperatures due to the reduction of non-radiative recombination processes. PL data from the quantum well samples clearly demonstrate the intensity increase. Figure 6.2 shows the temperature dependence of various emission peaks from the samples. Increases of up to three orders of magnitude have been recorded when the sample temperature was lowered from 300 to 30 K. As can be seen in the figure, the peak intensity saturates at low temperatures when the

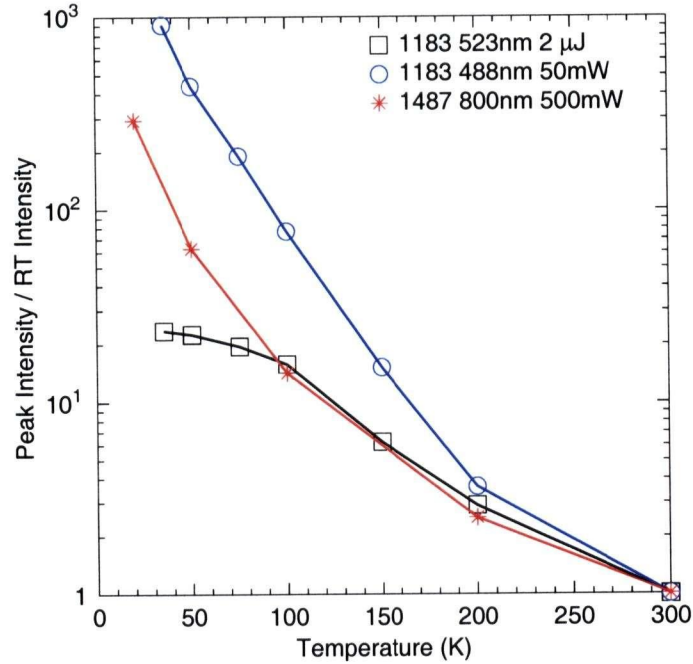


Figure 6.2: Peak emission intensity relative to room temperature intensity for various samples. Spectra excited by the pulsed laser experience low temperature saturation whereas CW excited spectra do not. The points from sample 1487 were taken from the short wavelength peak.

pulsed laser is used for excitation. When a CW laser is used, the intensity continues to grow as the sample temperature is lowered to the limit of our apparatus. The saturation in the pulse-excited PL spectra may be due to the conversion process approaching 100% quantum efficiency, presumably due to higher radiative recombination rates at high excitation levels.

Lowering the sample temperature also allows control of the relative intensities of the peaks from different quantum wells in the sample. Changing the temperature affects the ability of carriers to distribute themselves thermally amongst the wells, as discussed in section 3.2. Figure 6.3 shows PL from

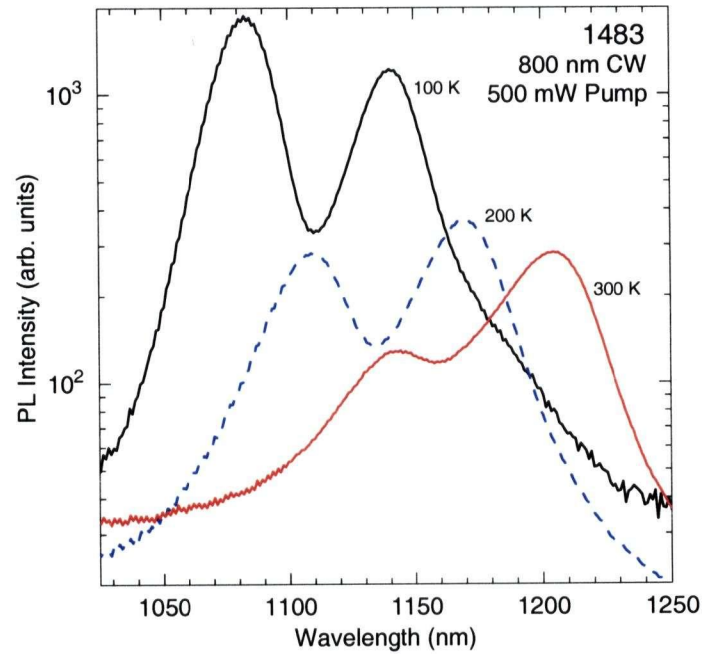


Figure 6.3: PL from double quantum well sample 1483. As the temperature increases, so does the relative intensity of the long wavelength peak.

a double quantum well sample. At room temperature the long wavelength peak is stronger, but as the temperature is lowered the shorter wavelength peak experiences a larger increase in intensity and eventually becomes the brighter feature. This is expected from rate-limited inter-well thermalization, but opposite to what one would expect from the Boltzmann factor. There is a competition between the Boltzmann distribution, which shows more preference for lower energy states at low temperatures, and the hopping between wells, which is greater at high temperatures. In this case, it seems that the hopping rate is the limiting factor. This effect will allow control over the shape of the emission spectrum in OCT source devices.

The ratio of emission peak intensities can be predicted using a rate equa-

tion model. If the carriers can enter the well via optical pumping, and leave the well through radiative recombination or transfer between wells, the rate of change of carrier population in the wells can be written as

$$\frac{dn_1}{dt} = P_1 - Bn_1^2 - \omega_1 n_1 + \omega_2 n_2 \quad (6.1a)$$

$$\frac{dn_2}{dt} = P_2 - Bn_2^2 - \omega_2 n_2 + \omega_1 n_1, \quad (6.1b)$$

where $n_{1,2}$ are the carrier concentrations in wells 1 and 2, $P_{1,2}$ are the pumping rates for the wells, B is the radiative recombination rate and the $\omega_{1,2}$ terms are the rates of transfer between wells. If the second well is deeper, then the rate of transfer to the shallower well should be small. If we assume that this contribution is negligible, we can eliminate the ω_2 terms.

If the system is in a steady state, the rates of change will be zero. Rearranging for n_1^2 and n_2^2 and dividing yields

$$\frac{n_2^2}{n_1^2} = \frac{P_2 B - \frac{\omega_1^2}{2} + \frac{\omega_1}{2} \sqrt{\omega_1^2 + 4P_1 B}}{P_1 B + \frac{\omega_1^2}{2} - \frac{\omega_1}{2} \sqrt{\omega_1^2 + 4P_1 B}}. \quad (6.2)$$

It is reasonable to assume that this ratio of the squares of the carrier concentrations in the wells is a good approximation to the ratio of peak emission intensities in the PL spectra. The ω_1 term can be written in terms of an activation energy such that

$$\omega_1 = \omega_0 e^{-\frac{U}{k_b T}}, \quad (6.3)$$

where ω_0 is an escape attempt frequency and U is the binding energy of the shallow quantum well. If we divide by $P_1 B$ and substitute

$$X = \frac{\omega_1}{\sqrt{P_1 B}}, \quad (6.4)$$

equation 6.2 can be rearranged to

$$\frac{n_2^2}{n_1^2} = \frac{\frac{P_2}{P_1} - \frac{1}{2}X^2 + \frac{1}{2}X\sqrt{X^2 + 4}}{1 + \frac{1}{2}X^2 - \frac{1}{2}X\sqrt{X^2 + 4}}. \quad (6.5)$$

The adjustable parameters are now $\frac{P_2}{P_1}$, $\frac{\omega_0}{\sqrt{P_1 B}}$ and U .

Figure 6.4 shows peak intensity ratio data from sample 1438 compared to a fit using equation 6.5. The model matches the curve well, and the parameters are realistic. The deep well was grown closer to the surface in this sample, so a pumping ratio of 1.8 seems reasonable. A rough estimate for $\frac{\omega_0}{\sqrt{P_1 B}}$ can be made as follows. The pumping rate for 20 ns, 2 μ J pulses incident on a 0.001 cm² spot will be around 10³⁰ cm⁻³/s assuming all the carriers are in a well. For $\omega_0 = 10^{11}$ Hz and $B = 10^{-10}$ cm³/s[82], $\frac{\omega_0}{\sqrt{P_1 B}}$ is about 10, similar to the calculated parameter.

These rate equations provide an experimental determination of a binding energy for the shallow quantum well. The quantum well model presented earlier predicts electron and hole binding energies of 167 and 42 meV, respectively, for this sample. The parameter U (best fit value 27 meV) could be related to the hole binding energy (42 meV) since it is similar.

6.3 Cluster State Emission

Photoluminescence data from our samples exhibit signs of the nitrogen clustering mentioned in section 2.3. D.A. Beaton analyzed the effects of N cluster emission from GaNAs bulk layers in his M.Sc. thesis[29]. There he found the lower energy emission from the in-gap states to be dominant at low temperatures when using a CW source for PL excitation. Using a pulsed source

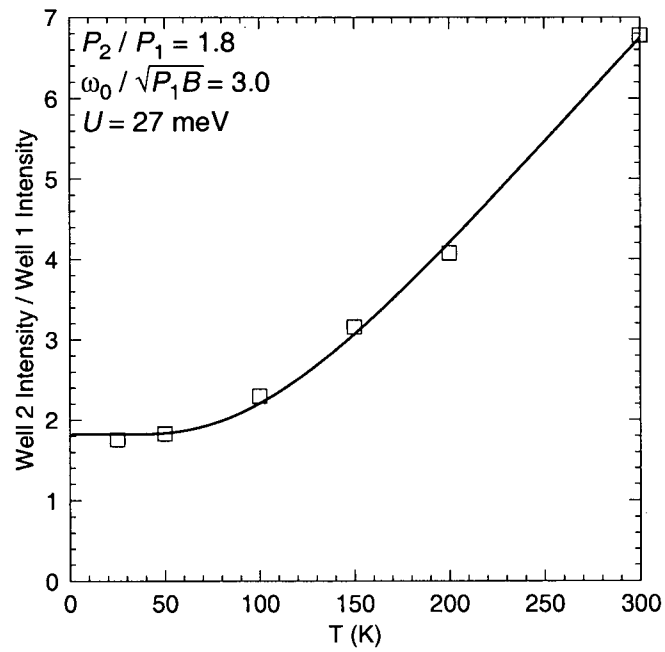


Figure 6.4: Ratio of low energy to high energy emission from the two quantum wells in sample 1438 (squares). The solid line is the fit from equation 6.5 with the indicated parameters.

reveals emission from band to band recombination in addition to the clusters, due to the higher photon densities and shorter carrier lifetimes. Short lifetimes give less time for carriers to be trapped by a cluster.

The quantum well samples grown for this work always showed dominantly interband emission, both for CW and pulsed excitation. Weak emission from the cluster states was present at times, but the predominance of band to band recombination suggests that quantum wells suppress cluster state effects. A possible explanation is that the two-dimensional nature of the well reduces the possibility for carriers to “find” a nitrogen cluster. The reduced dimensionality lowers the probability of carriers migrating to a cluster by chance.

If the diffusion length for the carriers is $\sqrt{D\tau}$, where D is the diffusion constant and τ is lifetime, the volume explored by a carrier in a bulk sample will increase at a rate proportional to $(D\tau)^{\frac{3}{2}}$ (since the volume of a sphere is proportional to its radius cubed). In contrast, a two-dimensional pancake-shaped volume in a quantum well increases according to $D\tau$ (since the area of a circle is proportional to the radius squared, and the thickness is fixed). This means that for a given diffusion constant, time, and N concentration, more space is explored in a bulk sample than in a quantum well, allowing greater opportunity to encounter a nitrogen cluster. The ratio of explored volumes can be estimated as follows, using the ambipolar diffusion constant given by[83]

$$D_a = \frac{p + n}{p/D_n + n/D_p}, \quad (6.6)$$

where n, p are the electron and hole concentrations and $D_{n,p}$ are the electron and hole diffusion constants ($D_{n,p} = \mu_{n,p}k_bT$). Assuming equal carrier con-

centrations and taking values of 8000 and $300 \frac{\text{cm}^2}{V_s}$ for the electron and hole mobilities[84], respectively, we find a diffusion constant, D_a , of $578 \text{ cm}^2/\text{s}$. If, for example, the lifetime is 10^{-9} s , then the characteristic length, $\sqrt{D\tau}$, is about $1.2 \mu\text{m}$. This leads to a ratio of around 160 between the spherical volume and the quantum well (for a 10 nm thick well). The long diffusion length could also explain why the PL peak from the deeply buried quantum well in sample 1437 was so intense.

Confinement in the quantum well region increases electron and hole densities. The theoretical exciton binding energy is four times larger in two-dimensional systems and the quantum well makes it more difficult for electron-hole pairs to separate spatially. As a consequence, radiative recombination rates increase, and the time available for a carrier to find a cluster is limited. Also, if the surrounding layers do not contain nitrogen, the quantum well boundary regions are less likely to contain clusters, simply because there are no N atoms just outside the well. These two factors should further decrease N cluster state emission in quantum wells compared to bulk samples.

Figure 6.5 shows emission from the double well samples 1483 and 1484. 1484 was grown with GaNAs cladding surrounding the wells while 1483 was not. The long wavelength emission from the clusters is stronger when the GaNAs layers are present. This is logical given that there is more N present in that system. In addition, the above argument concerning the boundaries of the wells no longer applies since there is now nitrogen in the layers surrounding the well. In both cases, the N cluster emission is reduced at higher temperatures, since carriers have more available energy to escape the traps; the probability of being in a trap is lower at high temperatures, since the

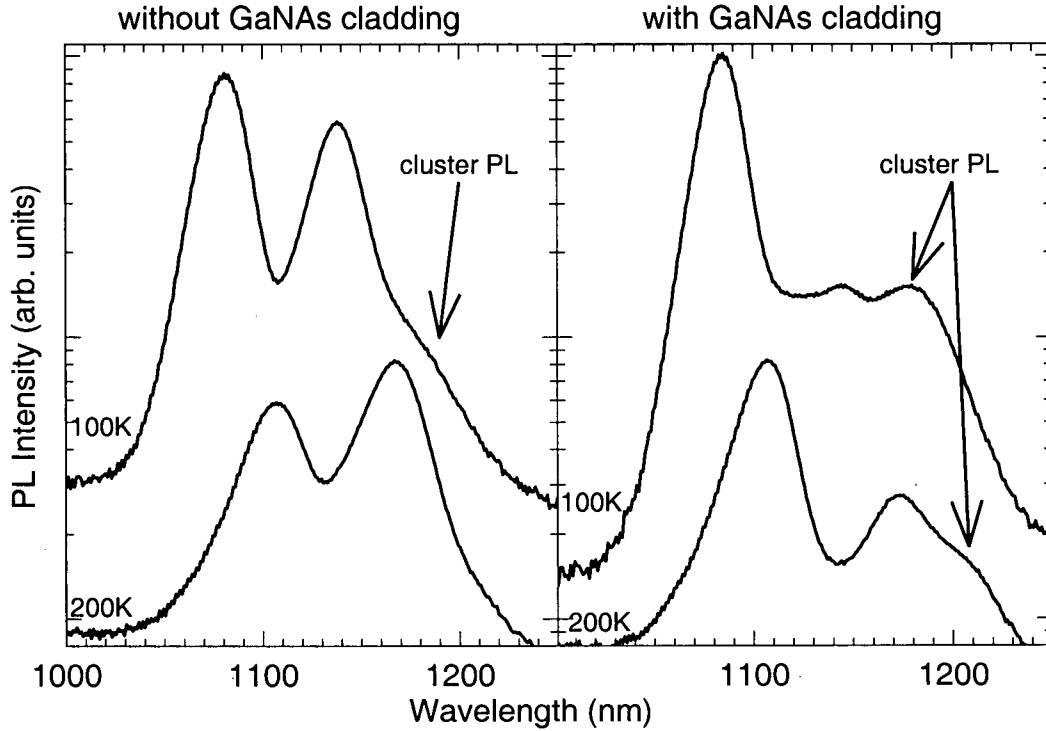


Figure 6.5: PL spectra from samples 1483 (left) and 1484 (right). Excitation is from the 800 nm CW diode pump operated at 250 mW. Cluster emission is more prevalent when GaNAs cladding layers are present.

Boltzmann factor is not as strong. Cluster emission falls off more slowly at higher temperatures when GaNAs cladding layers are present.

Although the broadening effects of N cluster emission are not a large concern in terms of the broadband aspect of the source, the reduction of these effects may make it easier to design a balanced output spectrum. The reasoning used above to explain the reduced N cluster emission in quantum well samples should also apply to carriers recombining at non-radiative centres, which should help to achieve the required intensities. These benefits of using

quantum well devices could eliminate several potential problems for the OCT source.

Chapter 7

Conclusion

Optical coherence tomography is a new medical technique with many possibilities. “Optical biopsies” would allow for more accurate and convenient diagnostic procedures. OCT can provide real-time monitoring of disease treatments, such as photodynamic therapy, and allows changes in blood flow to be visualized through the analysis of Doppler information.

Although some commercial OCT systems are currently available, especially those designed for ocular imaging, wide-scale deployment is currently restricted by the lack of a suitable low-cost light source. This work presents a GaInNAs semiconductor design for a new OCT source that should achieve the required emission bandwidth and intensity while being economical and convenient for use in a clinical setting.

A model for the composition dependence of the band gap of quaternary semiconductor compounds has been developed and applied to the GaInNAs and GaNAsBi systems. This one-parameter fitting technique provides a simple method for predicting the band gap for a wide range of compositions and can match experimental data with accuracies similar to more complicated techniques. The coupling parameter for In and N was found to be negative, indicating that the combination of the two alloying elements reduces the band gap less than the sum of their individual effects. The opposite

situation was found for Bi and N, where the coupling parameter was positive. A program that determines device emission energies based on quantum well compositions and thicknesses has been successfully used to predict and analyze prototype light source structures.

A series of multiple-quantum-well samples was grown by MBE and characterized with photoluminescence measurements. Broadband emission in the near-infrared was achieved, with FWHMs of close to 200 nm. Low temperature operation increased PL intensity by up to three orders of magnitude and allowed control over the relative heights of distinct emission peaks. A rate equation model has been developed to explain the temperature dependence of the relative peak intensities. Emission from nitrogen cluster states, which is dominant in bulk samples at low temperatures, was suppressed or eliminated in our GaInNAs quantum well devices.

Future work will involve fabricating devices with many more quantum wells in order to provide smoother emission spectra, a requirement for proper OCT imaging. Greater output intensities will be achieved by using high power optical pumping to enter the stimulated emission regime. Calculations have been presented that indicate that the effects of line narrowing on emission spectra, while significant, should not prevent the device from functioning properly. Waveguide layers will be added to the devices to provide confinement for the emitted photons. This will also greatly increase output power.

The presented design for a multiple-quantum-well semiconductor device successfully demonstrates the principles involved in the production of a new type of light source for OCT.

Bibliography

- [1] D. Huang, E.A. Swanson, C.P. Lin, J.S. Schuman, W.G. Stinson, W. Chang, M.R. Hee, T. Flotte, K. Gregory, C.A. Puliafito, and J.G. Fujimoto. *Science*, **254**:1178, 1991.
- [2] J.G. Fujimoto. *Nature Biotechnology*, **21**:1361, 2003.
- [3] J.G. Fujimoto. *Handbook of Optical Coherence Tomography*, chapter Optical Coherence Tomography: Introduction, page 1. Marcel Dekker, 2002.
- [4] B.E.A. Saleh and M.C. Teich. *Fundamentals of Photonics*. John Wiley & Sons, 1991.
- [5] B.E. Bouma and G.J. Tearney. *Handbook of Optical Coherence Tomography*, chapter Optical Sources, page 67. Marcel Dekker, 2002.
- [6] DenseLight Semiconductors. www.denselight.com, 2004.
- [7] A.Y. Cho. *The Technology and Physics of Molecular Beam Epitaxy*, chapter Introduction, page 1. Plenum Press, 1985.
- [8] U. Tisch, E. Finkman, and J. Salzman. *Applied Physics Letters*, **81**:463, 2002.

-
- [9] I.A. Buyanova, W.M. Chen, and B. Monemar. *MRS Internet Journal Nitride Semiconductor Research*, **6**:1, 2001.
 - [10] E. Tournié, N. Grandjean, A. Trampert, J. Massies, and K.H. Ploog. *Journal of Crystal Growth*, **150**:460, 1995.
 - [11] S. Tixier, M. Adamcyk, E.C. Young, J.H. Schmid, and T. Tiedje. *Journal of Crystal Growth*, **251**:449, 2003.
 - [12] S.R. Johnson and T. Tiedje. *Journal of Applied Physics*, **78**:5609, 1995.
 - [13] J.I. Pankove. *Physical Review*, **140**:A2059, 1965.
 - [14] D.G. Thomas and J.J. Hopfield. *Physical Review*, **150**:680, 1966.
 - [15] X. Liu, M.-E. Pistol, L. Samuelson, S. Schwetlick, and W. Seifert. *Applied Physics Letters*, **56**:1451, 1990.
 - [16] H. Grüning, L. Chen, Th. Hartmann, P.J. Klar, W. Heimbrodt, F. Höhnsdorf, J. Koch, and W. Stolz. *Physica Status Solidi B*, **215**:39, 1999.
 - [17] Y. Zhang, A. Mascarenhas, J.F. Geisz, H.P. Xin, and C.W. Tu. *Physical Review B*, **63**:085205, 2001.
 - [18] Y. Zhang, S. Francoeur, A. Mascarenhas, H.P. Xin, and C.W. Tu. *Physica Status Solidi B*, **228**:287, 2001.
 - [19] P.R.C. Kent and A. Zunger. *Physical Review B*, **64**:115208, 2001.
 - [20] P.R.C. Kent and A. Zunger. *Physical Review Letters*, **86**:2613, 2001.

-
- [21] P.R.C. Kent and A. Zunger. *Physica Status Solidi B*, **228**:253, 2001.
- [22] P.R.C. Kent, L. Bellaiche, and A. Zunger. *Semiconductor Science and Technology*, **17**:851, 2002.
- [23] P.R.C. Kent and A. Zunger. *Applied Physics Letters*, **82**:559, 2003.
- [24] H. Saito, T. Makimoto, and N. Kobayashi. *Journal of Crystal Growth*, **170**:372, 1997.
- [25] E. Nodwell, M. Adamcyk, A. Ballestad, T. Tiedje, S. Tixier, S.E. Webster, E.C. Young, A. Moewes, E.Z. Kurmaev, and T. van Buuren. *Physical Review B*, **69**:155210, 2004.
- [26] P. Wei, S. Tixier, M. Chicoine, S. Francoeur, A. Mascarenhas, T. Tiedje, and F. Schiettekatte. *Nuclear Instruments and Methods in Physics Research B*, **219** — **220**:671, 2004.
- [27] H.A. McKay, R.M. Feenstra, T. Schmidtling, and U.W. Pohl. *Applied Physics Letters*, **78**:82, 2001.
- [28] H.A. McKay, R.M. Feenstra, T. Schmidtling, U.W. Pohl, and J.F. Geisz. *Journal of Vacuum Science and Technology B*, **19**:1644, 2001.
- [29] D.A. Beaton. *Temperature Dependence of Photoluminescence of the Dilute Nitride Semiconductor GaN_xAs_{1-x}*. Master's thesis, University of British Columbia, 2003.
- [30] P. Perlin, S.G. Subramanya, D.E. Mars, J. Kruger, N.A. Shapiro, H. Siegle, and E.R. Weber. *Applied Physics Letters*, **73**:3703, 1998.

-
- [31] I.A. Buyanova, W.M. Chen, G. Pozina, J.P. Bergman, B. Monemar, H.P. Xin, and C.W. Tu. *Applied Physics Letters*, **75**:501, 1999.
- [32] K. Uesugi, I. Suemune, T. Hasegawa, T. Akutagawa, and T. Nakamura. *Applied Physics Letters*, **76**:1285, 2000.
- [33] A. Polimeni, M. Capizzi, M. Geddo, M. Fischer, M. Reinhardt, and A. Forchel. *Applied Physics Letters*, **77**:2870, 2000.
- [34] S. Shirakata, M. Kondow, and T. Kitatani. *Journal of Physics and Chemistry of Solids*, **64**:1533, 2003.
- [35] A. Polimeni, M. Capizzi, M. Geddo, M. Fischer, M. Reinhardt, and A. Forchel. *Physical Review B*, **63**:195320, 2001.
- [36] R. Dingle, W. Wiegmann, and C.H. Henry. *Physical Review Letters*, **33**:827, 1974.
- [37] C. Weisbuch and B. Vinter. *Quantum Semiconductor Structures: Fundamentals and Applications*. Academic Press, 1991.
- [38] S. Ikeda and A. Shimizu. *Applied Physics Letters*, **59**:504, 1991.
- [39] I.J. Fritz, J.F. Klem, M.J. Hafich, A.J. Howard, and H.P. Hjalmarson. *IEEE Photonics Technology Letters*, **7**:1270, 1995.
- [40] C.-F. Lin, B.-L. Lee, and P.-C. Lin. *IEEE Photonics Technology Letters*, **8**:1456, 1996.
- [41] C.-F. Lin and B.-L. Lee. *Applied Physics Letters*, **71**:1598, 1997.

-
- [42] X. Zhu, D.T. Cassidy, M.J. Hamp, D.A. Thompson, B.J. Robinson, Q.C. Zhao, and M. Davies. *IEEE Photonics Technology Letters*, **9**:1202, 1997.
- [43] M.J. Hamp, D.T. Cassidy, B.J. Robinson, Q.C. Zhao, and D.A. Thompson. *Applied Physics Letters*, **74**:744, 1999.
- [44] L.F. Bian, D.S. Jiang, S.L. Lu, J.S. Huang, K. Chang, L.H. Li, and J.C. Harmand. *Journal of Crystal Growth*, **250**:339, 2003.
- [45] H.Y. Liu, M. Hopkinson, P. Navaretti, M. Gutierrez, J.S. Ng, and J.P.R. David. *Applied Physics Letters*, **83**:4951, 2003.
- [46] W. Li, T. Jouhti, C.S. Peng, J. Konttinen, P. Laukkanen, E.-M. Pavlescu, M. Dumitrescu, and M. Pessa. *Applied Physics Letters*, **79**:3386, 2001.
- [47] A.Yu. Egorov, D. Bernklau, B. Borchert, S. Illek, D. Livshits, A. Rucki, M. Schuster, A. Kaschner, A. Hoffmann, Gh. Dumistras, M.C. Amann, and H. Riechert. *Journal of Crystal Growth*, **227** — **228**:545, 2001.
- [48] J.A. Gupta, P.J. Barrios, G.C. Aers, R.L. Williams, J. Ramsey, and Z.R. Wasilewski. *Solid State Electronics*, **47**:399, 2003.
- [49] D.E. Mars, D.I. Babic, Y. Kaneko, Y.-L. Chang, S. Subramanya, J. Kruger, P. Perlin, and E.R. Weber. *Journal of Vacuum Science and Technology B*, **17**:1272, 1999.
- [50] D.A. Livshits, A. Yu. Egorov, and H. Riechert. *Electronics Letters*, **36**: 1381, 2000.

-
- [51] S.G. Spruytte, M.C. Larson, W. Wampler, C.W. Coldren, H.E. Petersen, and J.S. Harris. *Journal of Crystal Growth*, **227 – 228**:506, 2001.
- [52] W. Ha, V. Gambin, M. Wistey, S. Bank, S. Kim, and J.S. Harris. *IEEE Photonics Technology Letters*, **14**:591, 2002.
- [53] E. Tournié, M.-A. Pinault, and A. Guzmán. *Applied Physics Letters*, **80**:4148, 2002.
- [54] M. Hetterich, M.D. Dawson, A.Yu. Egorov, D. Bernklau, and H. Riechert. *Applied Physics Letters*, **76**:1030, 2000.
- [55] T. Miyamoto, K. Takeuchi, F. Koyama, and K. Iga. *IEEE Photonics Technology Letters*, **9**:1448, 1997.
- [56] B. Borchert, A.Y. Egorov, S. Illek, and H. Riechert. *IEEE Photonics Technology Letters*, **12**:597, 2000.
- [57] E.-M. Pavelescu, C.S. Peng, T. Jouhti, J. Konttinen, W. Li, M. Pessa, M. Dumitrescu, and S. Spânulescu. *Applied Physics Letters*, **80**:3054, 2002.
- [58] L. Vegard. *Zeitschrift für Physik*, **5**:17, 1921.
- [59] M. Beaudoin, P. Desjardins, R.Y.-F. Yip, and R.A. Masut. *InP and Related Compounds: Materials, Applications and Devices*, volume 9 of *Optoelectronic Properties of Semiconductors and Superlattices*, chapter Optical and Structural Properties of InAsP/(Ga)InP Multilayers On InP(001): Strained-layer Multiple Quantum Well Structures and Devices, page 381. Gordon and Breach Science Publishers, 2000.

-
- [60] G.E. Pikus and G.L. Bir. *Soviet Physics Solid State*, **1**:136, 1959.
- [61] G.E. Pikus and G.L. Bir. *Soviet Physics Solid State*, **1**:1502, 1960.
- [62] H. Asai and K. Oe. *Journal of Applied Physics*, **54**:2052, 1983.
- [63] I. Vurgaftman and J.R. Meyer. *Journal of Applied Physics*, **94**:3675, 2003.
- [64] I. Vurgaftman, J.R. Meyer, and L.R. Ram-Mohan. *Journal of Applied Physics*, **89**:5815, 2001.
- [65] M.H. Gass, A.J. Papworth, T.B. Joyce, T.J. Bullough, and P.R. Chalker. *Applied Physics Letters*, **84**:1453, 2004.
- [66] A.G. Thompson and J.C. Woolley. *Canadian Journal of Physics*, **45**:255, 1967.
- [67] S. Francoeur, A. Mascarenhas, Y. Zhang, S. Yoon, M.J. Seong, M.C. Hanna, and J.F. Geisz. *On the origin of the band gap reduction in GaAsN*. Presentation, Vancouver, 2003.
- [68] K. Onabe, D. Aoki, J. Wu, H. Yaguchi, and Y. Shiraki. *Physica Status Solidi A*, **176**:231, 1999.
- [69] W.A. Harrison. *Electronic Structure and the Properties of Solids*. Dover, 1980.
- [70] R.L. Moon, G.A. Antypas, and L.W. James. *Journal of Electronic Materials*, **3**:635, 1974.

-
- [71] J.-Y. Duboz, J.A. Gupta, Z.R. Wasilewski, J. Ramsey, R.L. Williams, G.C. Aers, B.J. Riel, and G.I. Sproule. *Physical Review B*, **66**:085313, 2002.
- [72] A. Lindsay and E.P. O'Reilly. *Solid State Communications*, **118**:313, 2001.
- [73] T.H. Glisson, J.R. Hauser, M.A. Littlejohn, and C.K. Williams. *Journal of Electronic Materials*, **7**:1, 1978.
- [74] S. Tixier, M. Adamcyk, T. Tiedje, S. Francoeur, A. Mascarenhas, P. Wei, and F. Schiettekatte. *Applied Physics Letters*, **82**:2245, 2003.
- [75] A. Mascarenhas, Y. Zhang, J. Verley, and M.J. Seong. *Superlattices and Microstructures*, **29**:395, 2001.
- [76] A. Janotti, S.-H. Wei, and S.B. Zhang. *Physical Review B*, **65**:115203, 2002.
- [77] M. Yoshimoto, W. Huang, Y. Takehara, J. Saraie, A. Chayahara, Y. Horino, and K. Oe. *Japanese Journal of Applied Physics*, **43**:L845, 2004.
- [78] S. Francoeur, M.-J. Seong, A. Mascarenhas, S. Tixier, M. Adamcyk, and T. Tiedje. *Applied Physics Letters*, **82**:3874, 2003.
- [79] M. Adamcyk. *Epitaxial Growth of Dilute Nitride-Arsenide Compound Semiconductors by Molecular Beam Epitaxy*. PhD thesis, University of British Columbia, 2002.
- [80] A. Liptak. Private communication, 2004.

-
- [81] R.A. Serway, C.J. Moses, and C.A. Moyer. *Modern Physics: Second Edition*. Saunders College Publishing, 1997.
- [82] G.P. Agrawal and N.K. Dutta. *Long-Wavelength Semiconductor Lasers*. Van Nostrand Reinhold, 1986.
- [83] A. Many, Y. Goldstein, and N.B. Grover. *Semiconductor Surfaces*. North-Holland Publishing Company, 1965.
- [84] M. Balkanski and R.F. Wallis. *Semiconductor Physics and Applications*. Oxford University Press, 2000.